Neuron Derived Cytokine Interleukin-34 Controls Developmental Microglia Function

Benjamin A. Devlin[1], Dang M. Nguyen[1], Gabriel Grullon[1], Madeline J. Clark[2], Alexis M. Ceasrine[1], Martha Deja[1], Ashka Shah[1], Shomik Ati[1], Amelie Finn[1], Diogo Ribeiro[3], Anne Schaefer[3], Staci D. Bilbo*[1,2]

[1]Department of Psychology and Neuroscience, Duke University, Durham, NC, USA
[2]Departments of Neurobiology and Cell Biology, Duke University Medical Center, Durham, NC, USA
[3]Nash Family Department of Neuroscience, Icahn School of Medicine at Mount Sinai, New York, NY, USA

Abstract.

Neuron-microglia interactions dictate the development of neuronal circuits in the brain. However, the factors that support and broadly regulate these processes across developmental stages are largely unknown. Here, we find that IL34, a neuron-derived cytokine, is upregulated in development and plays a critical role in supporting and maintaining neuroprotective, mature microglia in the anterior cingulate cortex (ACC) of mice. We show that IL34 mRNA and protein is upregulated in neurons in the second week of postnatal life and that this increase coincides with increases in microglia number and expression of mature, homeostatic markers, e.g., TMEM119. We also found that IL34 mRNA is higher in more active neurons, and higher in excitatory (compared to inhibitory) neurons. Genetic KO of IL34 prevents the functional maturation of microglia and results in an anxiolytic phenotype in these mice by adulthood. Acute, low dose blocking of IL34 at postnatal day (P)15 in mice decreased microglial TMEM119 expression and increased aberrant microglial phagocytosis of thalamocortical synapses within the ACC. In contrast, viral overexpression of IL34 early in life (P1-P8) caused early maturation of microglia and prevented microglial phagocytosis of thalamocortical synapses during the appropriate neurodevelopmental refinement window. Taken together, these findings establish IL34 as a key regulator of neuron-microglia crosstalk in postnatal brain development, controlling both microglial maturation and synapse engulfment.

Introduction.

Microglia serve diverse roles in normal brain development including functions in vasculogenesis, neurogenesis, myelination, tissue repair, and synaptic remodeling[1]. Microglia are tissue-resident macrophages and progress through different functional stages in development[2] dependent upon

30 precise molecular cues they receive from other cells in their neural environment. These cues are still
31 being defined and likely depend on the distinct brain region and/or specific circuits within a given
32 region. In many brain regions, it is not until around the second postnatal week of life in mice that
33 microglia adopt a transcriptional and functional profile consistent with adult microglia[2,3]; however, little
34 is known about the timing of this transition, or the putative brain-specific signals that may contribute
35 to it[4].

36 As macrophages, microglia depend on signaling through the colony-stimulating factor 1 receptor
37 (CSF1r) for their proliferation, differentiation, and survival[5–7]. For this reason, CSF1r is often targeted
38 for microglial depletion experiments[8], and blockage or genetic knock-out of this receptor potently
39 reduces microglia number in the brain at every stage of development[9]. Often overlooked is the fact
40 that there are two known ligands that signal through this receptor: CSF1, which is expressed in all
41 tissues, and the more recently identified interleukin-34 (IL34), whose expression is limited to
42 keratinocytes in the skin and neurons in the forebrain[10,11]. Further, there is a spatio-temporal pattern
43 of microglial dependence on, and presence of, CSF1 and IL34. In the embryonic and early postnatal
44 mouse brain, CSF1 is predominantly expressed in all brain regions, and the loss of CSF1 alone is
45 sufficient to deplete virtually all microglia. This is in stark contrast to the adult brain, where IL34 is
46 expressed at higher levels in the forebrain, and as a result roughly 70-90% of gray matter microglia in
47 the forebrain depend on IL34 signaling for survival, while microglia in the cerebellum and brainstem
48 still depend on CSF1[7,10–13]. It is also notable that these signals come from different cellular sources,
49 as CSF1 is primarily expressed by microglia early in life[2] and later by oligodendrocytes and astrocytes,
50 while IL34 is expressed by neurons[13]. Thus, given these differences in timing, brain region, and cell
51 source, it is highly unlikely these two ligands play a redundant role for microglial survival and
52 differentiation, however no work to date has empirically tested this *in vivo*. There does exist some
53 preliminary evidence that CSF1 and IL34 drive distinct transcriptional programs in microglia[14], but it
54 is still unknown (1) when forebrain microglia become primarily dependent on IL34, (2) how neurons,

55 and which neurons, express IL34, and (3) how IL34 could differentially influence microglia cell state
56 and function, *in vivo*, in cortical development.

57 Here, we demonstrate that IL34 is developmentally upregulated in the second week of postnatal life
58 in mice in multiple forebrain regions. We show that IL34 expression in the cortex is regulated by
59 neuronal activity and is expressed at a higher level in glutamatergic (VGlut1+) neurons compared to
60 GABAergic (Gad2+) neurons. Constitutive genetic knock-out of IL34 impacts microglia numbers and
61 developmental cell state as demonstrated by decreased TMEM119 expression and increased
62 phagocytic capacity at P15. These microglial changes led to changes in ultrasonic vocalizations at
63 P15, as well as anxiety in adulthood. Acute, low-dose antibody blocking of IL34 at P15 prevents drastic
64 microglia loss, but still impacts microglial TMEM119 expression, decreases the amount of homeostatic
65 ($TMEM^{Hi}/CD68^{Lo}$) microglia, increases phagocytic microglia ($TMEM^{Lo}/CD68^{Hi}$), and increases
66 aberrant microglial phagocytosis of synapses. Finally, we show that viral overexpression of IL34 in
67 neurons at a developmentally inappropriate timepoint (P1-P8) prematurely increases microglial
68 TMEM119 expression and decreases microglial engulfment of synapses.

Results.

IL34 expression is regulated by development, neuronal activity, and subtype.

We first examined the time course of IL34 and CSF1 expression in the developing mouse brain. Previous literature has demonstrated that all microglia in the embryonic brain depend on CSF1 signaling for their survival, whereas microglia in the adult brain depend on either IL34 or CSF1, depending on the brain region[7,10–12]. Despite this, little was known about the timing of when IL34 becomes the primary signal for microglia in regions that show high levels of adult IL34 expression (cortex and striatum)[13]. To answer this, we collected brains from wild-type, C57Bl6/j male and female mice at 6 ages (postnatal day 7, 14, 20, 30, 38, 55) spanning early life, adolescence, and early adulthood in mice[15]. We took tissue punches from brain regions that are IL34-dependent in adulthood (Anterior Cingulate Cortex (ACC), Nucleus Accumbens (NAc), Amygdala (AMY)) and from a CSF1-dependent region (Cerebellum (CBM)) and measured IL34 and CSF1 mRNA levels using qPCR (Figure 1a). While we found no significant developmental expression pattern of CSF1 mRNA in any of the regions, we did find a striking developmental increase in IL34 mRNA, which began between postnatal day 7 (P7) and P14 in all forebrain regions, while IL34 remained at low levels in the cerebellum (Figure 1b). To test whether this increase in IL34 mRNA corresponded to an increase in protein, we collected another cohort of mice at the ages of the initial increase (P8 and P15) and used ELISA to measure total IL34 protein in the ACC. We focus on ACC in all following experiments, as ACC is a cortical region with high levels of IL34 in adulthood, and previous work in our lab has detailed a developmental period of microglia-neuron interactions in this brain region[16]. We observed a marked increase in IL34 protein between the first and second week of postnatal life in the ACC, while there was no such increase in the cerebellum (Figure 1c). Together, these results suggest that IL34 expression increases in the ACC in the second postnatal week.

Next, we became interested in the neuronal mechanisms that regulate the expression of IL34. We hypothesized IL34 expression in neurons may be regulated by neuronal activity, in part because the observed upregulation of IL34 in the ACC in the second postnatal week of life paralleled our previous

finding that this was a period of excitatory synaptogenesis in the ACC[16]. Additionally, it has been shown that IL34-dependent striatal microglia are sensitive to neuronal activity[13], while CSF1-dependent microglia are not. To test this, we artificially manipulated neuronal activity in the early neonatal window by injecting a virus expressing a GFP reporter (pAAV8-hSyn-eGFP) or a virus encoding the excitatory designer receptor exclusively activated by designer drug (DREADD) receptor hM3D(Gq) (pAAV8-hSyn-hM3D(Gq)-mCherry) into the frontal cortex of mice at postnatal day 1 (Figure 1d). These viruses were driven by the human synapsin-1 promoter, which reliably transduces and leads to the expression of the designer receptor in all neurons. We then injected the designer drug deschloroclozapine (DCZ) at postnatal day 8, 9, and 10. We confirmed that this approach reliably activated neurons in Gq-expressing mice compared to GFP controls by measuring Fos expression at the mRNA and protein level (Supp. Fig. 1a-d). Using RNAScope, we stained and quantified IL34 mRNA and initially found no difference in total IL34 levels between GFP control and Gq mice (Supp. Fig. 1e-f). This quantification, however, did not take into consideration IL34 expression based on activity level or viral transduction status within individual neurons. Furthermore, viral expression in these experiments was driven by the synapsin-1 promoter, which transduces both excitatory and inhibitory neurons, introducing potential complications when it comes to measuring total circuit activity. To overcome these technical issues, we used a panel of mRNA probes that allowed us to distinguish between active (Fos+, i.e. greater than 6 Fos puncta per cell adjusted for cell size) or inactive (Fos-), and GABAergic (Gad2+) or glutamatergic (Gad2-) neurons to quantify IL34 mRNA expression at a single-cell resolution (Figure 1e). When we quantified the number of IL34 mRNA puncta in Fos+ (active) compared to Fos- (inactive) neurons in Gq mice, we found significantly higher expression of IL34 in Fos+ neurons (Figure 1f). We also observed a trending increase in IL34 puncta in Fos+ neurons in GFP control mice (Supp. Fig. 1g). Additionally, we observed a positive correlation between the average number of IL34 puncta and average number of Fos puncta per cell per animal (Figure 1g). This correlation was driven by Gad2-, presumably excitatory, neurons (Supp. Fig. 1h). Thus, as a follow-up experiment, we stained the tissue with a second set of mRNA probes to quantify IL34

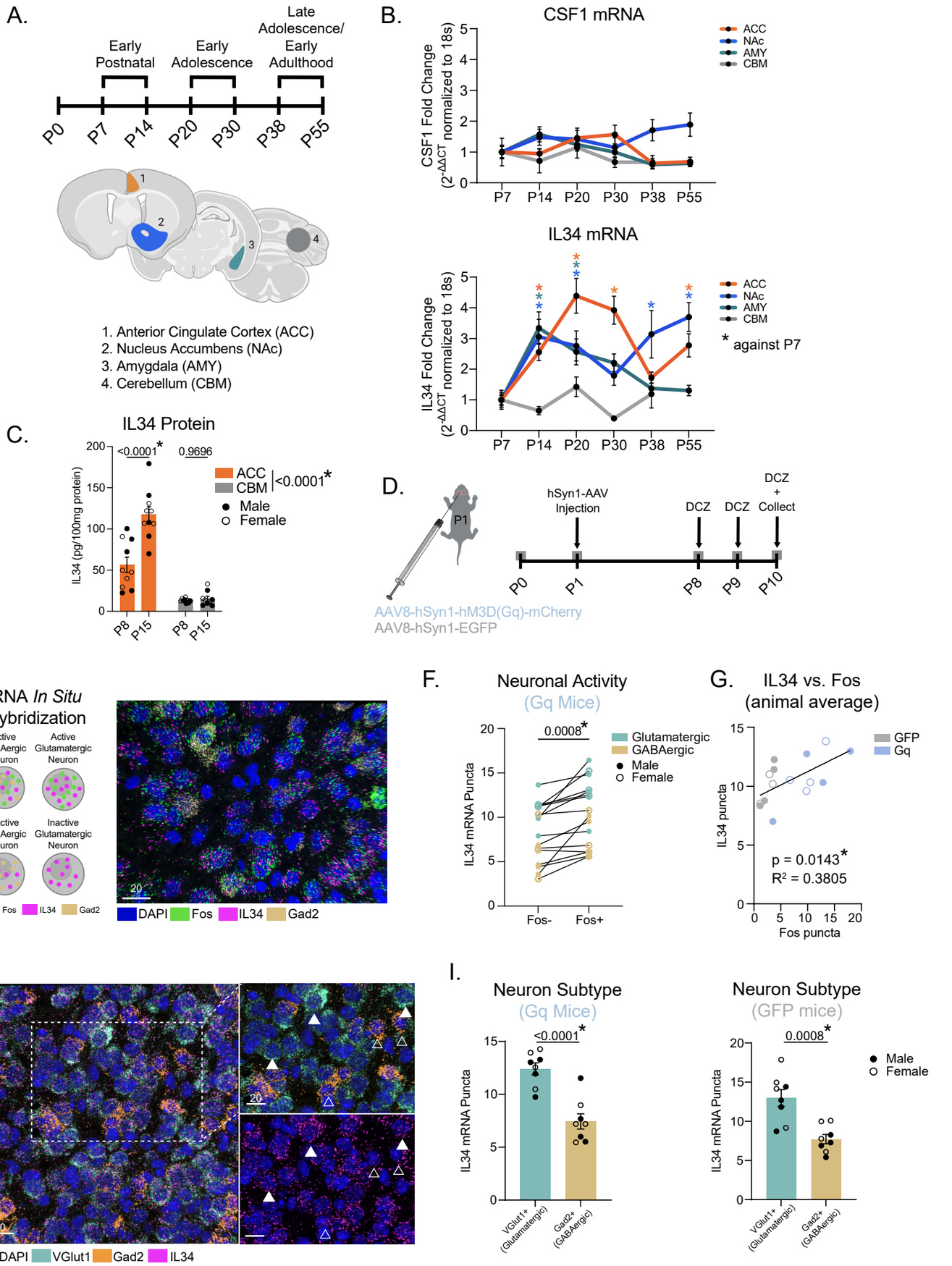

Figure 1. IL34 is regulated by development, neuronal activity, and neuronal subtype.
(A) Experimental timeline for WT brain collection across development and diagram of brain regions tissue punched for qPCR analysis.
(B) Quantification of IL34 and CSF1 mRNA levels in all four brain regions across six postnatal developmental timepoints. (n = 8 male and 8 female C57Bl6/j wild-type mice/age, P55 cerebellum excluded due to poor RNA quality, one-way ANOVA , data normalized to P7).
(C) Quantification of IL34 protein using ELISA from tissue punches of the ACC and CBM in a separate cohort of mice. (n = 5 male and 5 female C57Bl6/j wild-type mice/age, two-way ANOVA age x brain region, p values shown are from Sidak's *post hoc* test, main effect of brain region shown in legend).
(D) Experimental timeline for early postnatal viral injections and DREADDs experiments.
(E) Schematic outlining the different cell types identified by expression of IL34, Gad2, and Fos using RNA-FISH and representative image of RNA-FISH stain for Fos and IL34 showing IL34 levels in both Fos+ (active) neurons as well as Fos- (inactive) neurons.
(F) Quantification of IL34 mRNA puncta in Fos- and Fos+ cells in mice that received the Gq virus. (n = 4 mice/sex, data shown are a per animal average of the expression level of all neurons of that type (excitatory vs. inhibitory, and active vs. inactive, total of 5,722 cells analyzed), p value shown is from a paired t-test).
(G) Correlation between IL34 puncta and Fos puncta in GFP control and Gq mice. (n = 3-4 mice/sex/virus, data shown is a per animal average of IL34 and Fos puncta in all neurons, p value shown is from a pearson correlation).
(H) Representative image of second RNA-FISH stain including VGlut1 to distinguish excitatory neurons from inhibitory neurons more precisely.
(I) Quantification of IL34 mRNA puncta in excitatory (VGlut1+) and inhibitory (Gad2+) neurons in all mice. (n = 3-4 mice/sex/virus, data shown are a per animal average of the expression level of all neurons of that type (excitatory vs. inhibitory, total of 5,010 cells analyzed), p value shown is from an unpaired t-test). All data are mean ± s.e.m. All p-values that fall below p<0.05 are denoted with an asterisk

121 expression more precisely in glutamatergic (VGlut1+, excitatory) and GABAergic (Gad2+, inhibitory)
122 neurons and found that IL34 was about two-fold higher in excitatory neurons compared to inhibitory,
123 regardless of virus, biological sex, or activation (Fos+) status. Also of note, we saw a similar
124 percentage of active vs. inactive cells in excitatory and inhibitory neurons (Supp. Figure 1d). These
125 data indicate that, at the gene expression level, IL34 is regulated by neuronal activity and subtype in
126 the postnatal day 10 mouse cortex.

127 **Constitutive IL34 knock-out (KO) decreases adult microglial number and TMEM119**
128 **expression.**

129 Previous reports have demonstrated that adult mice lacking IL34 ($IL34^{LacZ/LacZ}$) have fewer microglia
130 in the cortex, striatum, and hippocampus, but not the cerebellum or brainstem[10,11]. We confirmed
131 these findings in $IL34^{LacZ/LacZ}$ adult male and female mice, and observed a moderate, yet significant,
132 reduction in Iba1+ cell number in $IL34^{LacZ/+}$ heterozygous mice, which has not been reported (Supp.
133 Figure 2a-b). We also observed that microglial numbers in the cortex and striatum of IL34 KO mice
134 were equivalent to cerebellar and brainstem microglia numbers, suggesting that, when IL34 is
135 constitutively lost, CSF1 continues to maintain a CSF1-dependent population of microglia in these
136 regions[13]. Interestingly, when staining for TMEM119, a microglia-specific marker that is
137 developmentally regulated and immunoreactive only in mature, homeostatic microglia[3,17], we found a
138 significant reduction in the expression of this protein in the remaining microglia of $IL34^{LacZ/LacZ}$ mice,
139 suggesting that these forebrain, CSF1-dependent microglia are immature and non-homeostatic
140 (Supp. Figure 2c). This diminished TMEM119 expression level in IL34 KO microglia was again similar
141 to the low level of expression seen in CSF1-maintained brainstem and cerebellar microglia, consistent
142 with the microglia number changes (Supp. Fig. 2d). In line with the hypothesis that there is a
143 developmental and potentially functional consequence of IL34 loss on microglia, we re-analyzed bulk
144 RNA-Sequencing on isolated microglia from the forebrain of WT and IL34 KO mice[14]. We found that
145 IL34 KO microglia from the forebrain were enriched for marker genes of neonatal microglia (ITGAX,
146 APOE, CLEC7A, LPL) while these cells had low expression of adult marker genes (P2YR12,

147 TMEM119, OLFML3, SIGLECH) compared to WT controls[2,3,18] (Supp. Fig. 3a). Notably, IL34 KO
148 microglia had a significant upregulation of CSF1 compared to WT controls, which has been shown to
149 be developmentally regulated[2,19], and suggests that, in the absence of the primary signal (IL34),
150 microglia have the capacity to upregulate CSF1 as a potential compensatory mechanism. These gene
151 expression changes were not observed to the same degree in the forebrain of CSF1 KO mice.
152 Additionally, many genes associated with microglia phagocytosis were significantly dysregulated in
153 forebrain IL34 KO microglia (C3AR1, ITGAM, AXL)[20–22](Supp. Fig. 3b). Thus, these data suggest that
154 when IL34 signaling is lost, the remaining Csf1-dependent microglia in forebrain resemble cerebellar
155 and brainstem CSF1-dependent microglia and have potentially disrupted phagocytic capabilities. This
156 supports the idea that there are distinct IL34- and CSF1-maintained subpopulations of microglia that
157 are transcriptionally/functionally distinct from each other, either based on IL34/CSF1 signaling or
158 based on their localization/cues from neighboring cells.

159 **IL34 KO impacts microglia state in the second postnatal week.**

160 Our observation that IL34 increases in the second postnatal week coincides with many known
161 developmental microglial processes in the forebrain, including proliferation[16], upregulation of
162 TMEM119[3], increased ramification[23], establishment of region-specific heterogeneity[24], and closure of
163 a period of synaptic pruning in the ACC[16]. To test the hypothesis that IL34 may be functionally
164 controlling these processes, we collected IL34$^{LacZ/+}$ (control) and IL34$^{LacZ/LacZ}$ (KO) mice at postnatal
165 day 8 (before the peak in IL34 expression) and postnatal day 15 (after the IL34 expression increase).
166 We first confirmed the developmental increase in IL34 expression by staining for LacZ in heterozygous
167 control mice (IL34$^{LacZ/+}$), and indeed saw robust reporter expression only at P15 in the ACC of these
168 mice (Figure 2a). We then used Iba1 staining in the ACC to count microglia number and quantify
169 microglia morphology, TMEM119 staining to assess microglial developmental maturation, and CD68
170 staining (lysosomal marker) to quantify microglial phagocytic capacity. When measuring overall cell
171 number, we found that IL34 KO mice had a reduction in Iba1+ microglia at both P8 and P15 (Figure
172 2b-c). When analyzing microglial process complexity using 2D sholl analysis, we found a significant

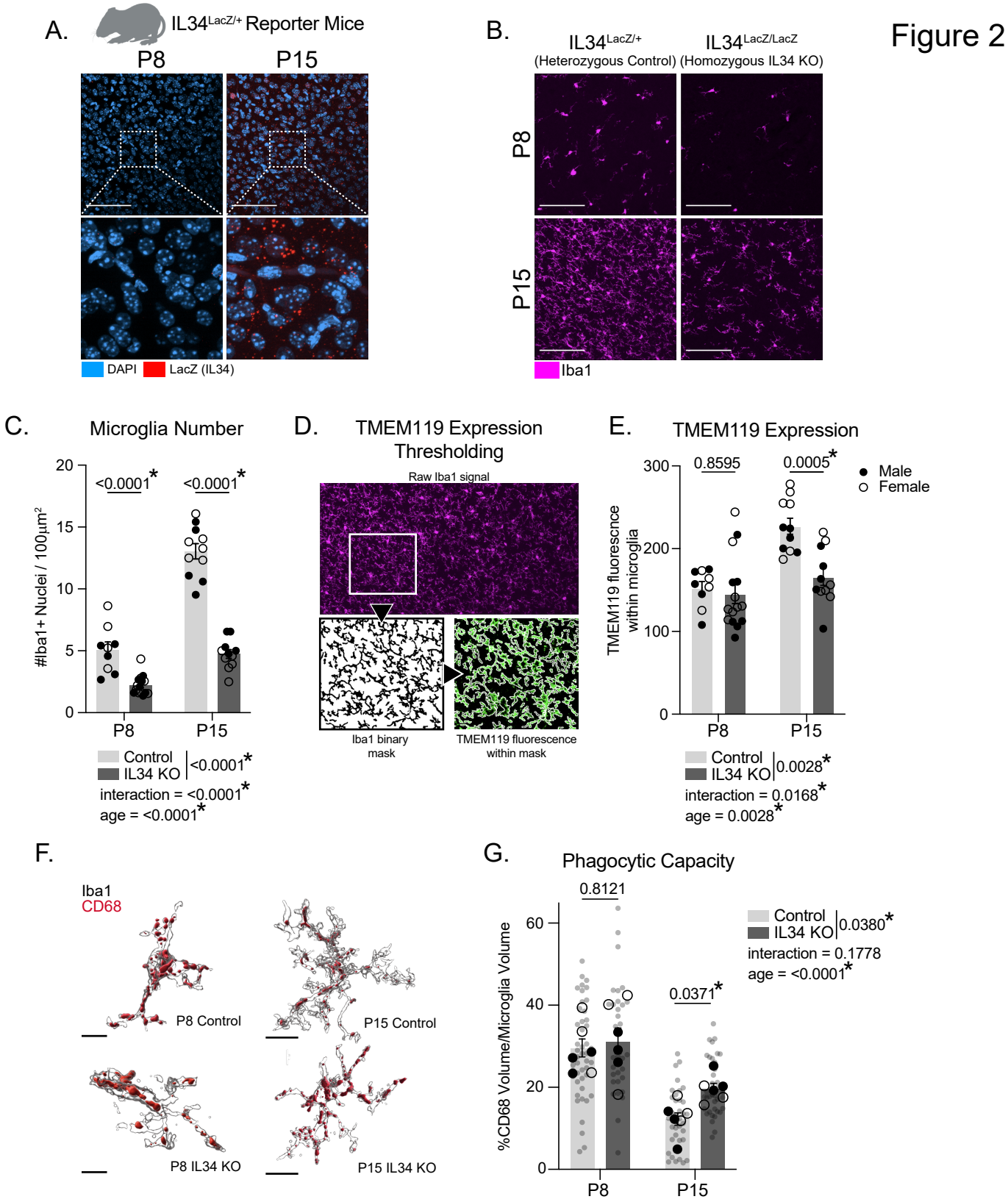

Figure 2. Constitutive IL34 KO impacts microglia in the second postnatal week.
(A) Representative image of LacZ immunostain in the ACC of IL34$^{LacZ/+}$ reporter mice at postnatal day 8 (P8) and P15 confirms robust increase in IL34 expression in the second postnatal week.
(B) Representative images of Iba1 immunostain in the ACC of P8 and P15 IL34$^{LacZ/LacZ}$ (IL34 KO) and IL34$^{LacZ/+}$ (Heterozygous control) mice. Scale = 100µm.
(C) Quantification of microglia numbers in the ACC of P8 and P15 IL34 KO and Control mice (n = 5-8 mice/sex/age/genotype, data shown are an average of 3 images taken from 3 sections of each mouse, two-way ANOVA age x genotype, p values shown over bars are from Sidak's post-hoc test, main effect of genotype and interaction term shown in legend).
(D) Method used for masking the Iba1 channel to quantify TMEM119 fluorescence only within microglia
(E) Quantification of TMEM119 mean gray value in the ACC of P8 and P15 IL34 KO and Control mice (n = 5-8 mice/sex/age/genotype, data shown are an average of 3 images taken from 3 sections of each mouse, two-way ANOVA age x genotype, p values shown over bars are from Sidak's *post-hoc* test, main effect of genotype and interaction term shown in legend).
(F) Representative IMARIS 3D reconstructions of microglia (Iba1) and lysosomes (CD68) co-immunostain from the ACC of P8 IL34 KO and Control mice. Scale = 5µm for P8 microglia, 15µm for P15 microglia.
(G) Quantification of phagocytic index (volume of CD68 / total microglia volume * 100) of microglia from the ACC of P8 and P15 IL34 KO and Control mice (n = 3 mice/sex/age/genotype, 4-6 cells analyzed per mouse, individual microglia represented by gray circles, animal averages represented by black dots, two-way ANOVA age x genotype, p values shown over bars are from Sidak's *post-hoc* test, main effect of genotype and interaction term shown in legend). All data are mean ± s.e.m. All p-values that fall below p<0.05 are denoted with an asterisk.

173 decrease in ramification in IL34 KO microglia only at P15 (Supp. Fig. 4a-c). To measure TMEM119
174 expression on a per cell basis in these mice, we calculated fluorescence intensity within Iba1 signal.
175 We first generated a binary mask of the Iba1 channel and then applied that mask to the TMEM119
176 channel before calculating mean gray value (Figure 2d). This prevented the obvious confound of
177 microglia number loss on total mean gray value quantification. When we quantified TMEM119 in this
178 manner, we found a significant reduction in TMEM119 protein expression in IL34 KO ACC microglia
179 only at P15 (Figure 2e), suggesting that IL34 is necessary for the developmental upregulation of this
180 protein in cortical microglia. We also observed a marked reduction in expression of another
181 homeostatic protein (P2YR12) at both P8 and P15 (Supp. Fig. 4d). We then assessed whether
182 microglia in IL34 KO mice had dysregulated phagocytic function, given that this window of
183 development corresponds to a period of microglial synaptic pruning previously described[16]. To
184 measure phagocytic capacity, we calculated the percent volume of the microglia (Iba1) containing
185 CD68 (lysosome) and found that at P15, but not P8, microglia in IL34 KO mice had elevated
186 phagocytic capacity compared to control (Figure 2f-g). Cell volume was also larger in the IL34 KO
187 microglia only at P15 (Supp. Fig. 4e). These findings are in line with the sequencing data (Supp. Fig.
188 4b) that showed many differentially expressed phagocytic receptors on microglia from IL34 KO mice.
189 It must be noted that one limitation of these findings is that there is significant reduction in the overall
190 number of microglia in IL34 KO mice (Figure 2b-c), and thus it is reasonable to assume that the
191 remaining microglia may be responding to this change, to functionally compensate for less microglia.
192 Nevertheless, these results suggested to us that IL34's role in the brain extends beyond controlling
193 microglial survival and has developmentally relevant functions for microglial maturation and
194 phagocytic capacity.

195 **IL34 KO does not impact microglia in the brainstem, or neuron, astrocyte, or oligodendrocyte**
196 **numbers in ACC.**

197 To determine the specificity of our microglia endpoints in the ACC, we tested whether IL34 KO
198 impacted microglia number, TMEM119 expression, and/or P2YR12 expression in the brainstem. We

199 found no effect of genotype on any of these endpoints in brainstem microglia at P8 or P15, suggesting
200 that these changes are not brain wide and may be more limited to forebrain, or potentially cortical,
201 microglia (Supp. Fig. 5a-c). Additionally, to determine the potential effects of IL34 knockout on cell
202 types in the brain other than microglia, we counted total numbers of neurons, astrocytes, and
203 oligodendrocytes in the ACC of IL34 KO and control mice at P8 and P15 (Supp. Fig. 5d). We found
204 no effect of genotype on neuron (NeuN+), astrocyte (Sox9+), or oligodendrocyte (Olig2+) cell numbers
205 (Supp. Fig. 5e-g). These data confirm that IL34 genetic KO primarily impacts microglia in the forebrain
206 and not the brainstem, and does not affect the overall number of neurons, astrocytes, or
207 oligodendrocytes, which is consistent with previous literature[5,10].

208 **IL34 KO imparts an anxiolytic phenotype at P15 and young adulthood.**

209 We next determined whether the functional changes to microglia we observed influenced behavioral
210 outcomes in these mice. We tested mice in a battery of behavioral paradigms during development
211 and in adulthood (Supp. Fig. 6a). We first tested the IL34 KO mice for changes in neonatal ultrasonic
212 vocalizations (USVs), which have been shown to be developmentally regulated in the second week
213 of postnatal life[16,25]. More specifically, previous work in the lab has found that P8 is the peak period
214 of calling for C57BL6/j mice, and has demonstrated that microglial perturbations early in life can impact
215 this behavior[16,25]. To evoke neonatal USVs, we briefly remove the pups from their nest and record
216 their vocalizations using a condenser microphone in a sound-isolated chamber for 3 minutes (Figure
217 3a). When we tested IL34 KO mice compared to littermate controls we found no difference in call
218 number at P8 but did find a significant decrease in both the number and energy of calls in P15 KO
219 mice (Figure 3b & Supp. Fig. 6b-c). To further analyze any potential structural changes in the
220 vocalizations, we used a machine-learning tool, Mouse Ultrasonic Profile ExTraction (MUPET)[26] to
221 classify calls into unique syllable repertoire groups (Figure 3c). When analyzing the similarity in call
222 structure between groups we found a high degree of similarity (88%) at P8, but a far lower similarity
223 (58%) between call structures at P15 (Figure 3d-e), indicating that the few calls they did make were
224 structured differently. These structural differences were present for both short and long call types

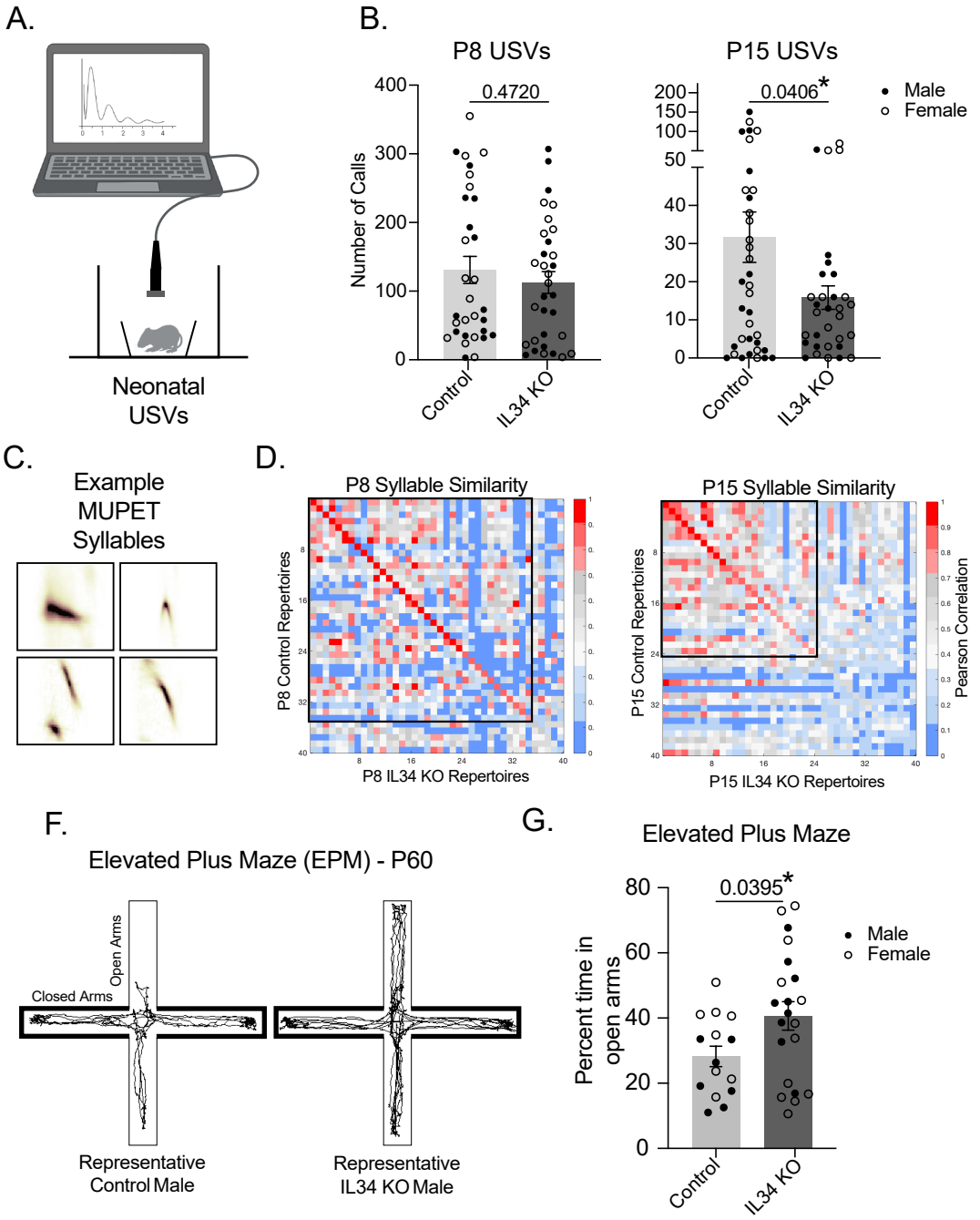

Figure 3. IL34 KO impacts neonatal ultrasonic vocalizations (USVs) at P15 and anxiety in adulthood.
(A) Schematic representation of USV collections done at P8 and P15 and MUPET analysis for syllable creation and comparison.
(B) Quantification of the total number of calls made over the three-minute isolation period at P8 and P15 in IL34 KO and control mice. (n = 16-18 mice/sex/genotype, p values shown are from unpaired t tests).
(C) Example USV syllables calculated using Mouse Ultrasonic Profile ExTraction (MUPET).
(D) MUPET syllable similarity heatmaps calculated from the USVs from P8 and P15 IL34 KO and Control mice. Repertoire similarity is calculated between Het and KO mice using Pearson correlation. Black box shows total number of repertoire units that are similar (0.8 Pearson correlation coefficient or above) between the two genotypes.
(E) Representative movement traces in the Elevated Plus Maze test in adult Control and IL34 KO mice.
(F) Quantification of percent time spent in open arms of the EPM (time spent in open arms / total test time * 100). (n = 6-12 mice/sex/genotype, p value shown is from an unpaired t test). All data are mean ± s.e.m. All p-values that fall below $p<0.05$ are denoted with an asterisk.

225 (Supp. Fig. 3d-e). We also found that IL34 KO mice had increased weight at both P8 and P15 (Supp.
226 Fig. 6f-g) but did not observe a difference in locomotor activity in the open field at P55, nor a change
227 in sociability at P65 (Supp. Fig. 6h-i). When we tested for anxiety in adulthood using the elevated plus
228 maze, we saw an increase in the percentage of time spent in the open arms in IL34 KO mice (Figure
229 3f-g), suggesting an anxiolytic phenotype in the KO mice. Finally, we used Barnes maze to measure
230 spatial memory and cognitive flexibility in males and found a significant increase in the number of
231 errors made by IL34 KO male mice only during the two reversal days (Supp. Fig. 6j-k), perhaps
232 suggesting these mice have a moderate deficit in cognitive flexibility. Taken together, IL34 KO has an
233 anxiolytic phenotype that begins at P15 (reduction in isolation-induced vocalizations) and persists to
234 adulthood (increased time in the open arms of the elevated plus maze). These findings make sense
235 given the ACC's role in regulating anxiety[27], and suggest that in addition to changes at the microglial
236 level, IL34 KO impacts behavior both early in life and in adulthood.

237 **Acute IL34 inhibition at P15 mimics constitutive genetic loss of IL34 and increases phagocytic**
238 **microglia.**

239 Our data thus far provide evidence for a developmental role of IL34 in controlling microglia function in
240 the second week of postnatal life. Additionally, previous literature has shown[10,11], and we have
241 replicated in our mice (Figure 2b-c, Supp. Fig. 3a-b), that genetic loss of IL34 drastically reduces the
242 number of surviving microglia in the cortex of the adult mouse brain to 30% of normal levels. Thus, in
243 order to control for any off-target developmental effects, or potential effects due to a major loss of
244 microglia, we injected function blocking antibodies against IL34 or CSF1[12] directly into the brain
245 intracerebroventricularly (I.C.V) to block IL34 (anti-IL34) or CSF1 (anti-CSF1) signaling in a temporally
246 precise manner at P15 (Figure 4a). This allowed us to titrate the dose of the antibody compared to
247 the previously published dose (1mg/kg in our study vs. 100mg/kg[12]) to reduce microglial cell death.
248 Indeed, when we collected these mice 48 hours after surgery, we found only a trending decrease in
249 the number of microglia in the ACC of these mice (Figure 4b-c), while we still saw a significant
250 decrease in TMEM119 expression in ACC microglia from anti-IL34-treated mice (Figure 4d). We also

251 replicated the decrease in ramification in anti-IL34 mice that we first observed in the constitutive
252 genetic KO (Supp. Fig. 7a). In our next set of experiments, we tested whether the decrease in
253 TMEM119 expression in anti-IL34 microglia was correlated with the increased expression of CD68.
254 We noticed significant microglial heterogeneity in that some cells were abnormally high in CD68
255 (suggestive of heightened phagocytic activity) and in turn low in TMEM119 (Figure 4e). We quantified
256 this heterogeneity by measuring and binning expression of the two markers on a per cell basis into
257 three categories: “Lo”, “Mid”, and “Hi” based on histograms of all fluorescence values in our dataset
258 (Supp. Fig. 7b-c) and calculating the percentage of cells analyzed from each animal that fell into “Hi”
259 and “Lo” categories. We found that in the anti-IL34 group, these mice had far fewer microglia that
260 were $CD68^{Lo}$ and $TMEM119^{Hi}$, an expression profile typical of homeostatic cortical microglia at P15
261 (Figure 4f). Conversely, when we quantified the percentage of phagocytic, non-homeostatic cells that
262 were $CD68^{Hi}$ and $TMEM119^{Lo}$, we found significantly more microglia in the IL34-blocked group that
263 fell into this category (Figure 4g). We also found a significant decrease in $TMEM^{Hi}$ cells and a trending
264 increase in $CD68^{Hi}$ cells (Supp. Fig. 8d-e). The results from these experiments suggest that preventing
265 IL34 signaling acutely at P15 is sufficient to phenocopy the effects seen in the constitutive genetic KO
266 and induce phagocytic, immature microglia. We acknowledge the limitations that come along with
267 injecting blocking antibodies surgically, which potentially causes tissue damage and microglia
268 activation. However, we feel confident in these data since they corroborate the findings from the non-
269 invasive, constitutive IL34 KO mice.

270 **Acute IL34 inhibition does not cause mass microglia death and repopulation.**

271 To validate that the phagocytic, immature microglia we captured in the anti-IL34 treatment were not
272 newly born microglia repopulating after potential mass microglial death that we were missing in the
273 time between surgery and collection 24 hours later, we generated a new cohort of
274 $P2yr12^{CreER/+}$;$tdtomato^{fl/+}$ mice to transiently tag microglia as RFP+ pre-surgery using 4-
275 hydroxytamoxifen (4OHT). We injected mice once with 75mg/kg 4OHT at P14, then injected either
276 control IgG or anti-IL34 antibodies ICV at P15 and collected the mice 48 hours later at P17 (Supp.

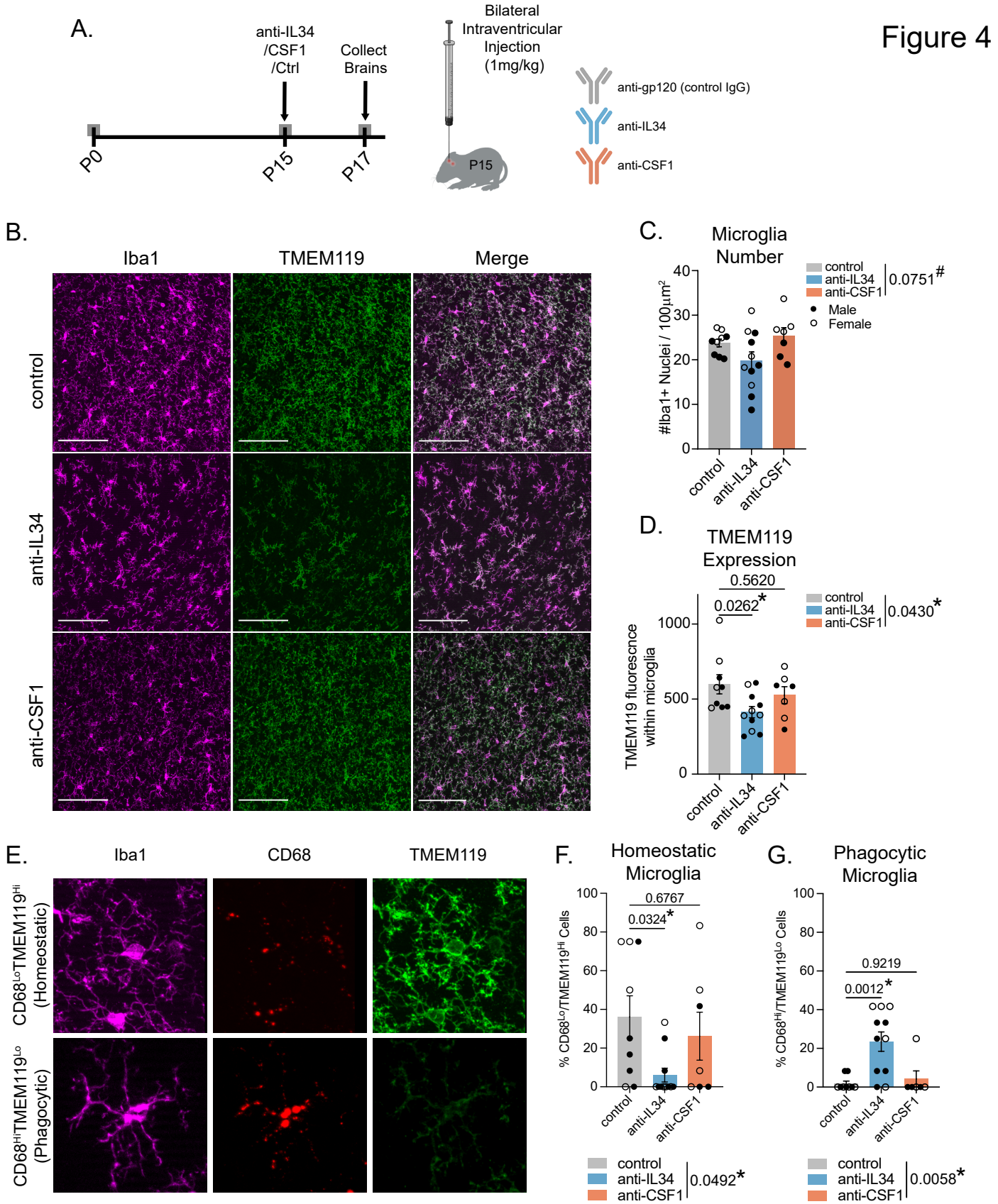

Figure 4. Acute IL34 inhibition at P15 mimics constitutive genetic loss of IL34 and increases phagocytic microglia.
(A) Experimental schematic of blocking antibody injection surgeries and tissue collection.
(B) Representative images of Iba1 and TMEM119 co-immunostain in the ACC of mice administered either control (IgG) antibody, anti-IL34, or anti-CSF1. Scale = 100µm.
(C) Quantification of microglia numbers in the three groups. (n = 3-6 mice/sex/antibody, data shown are an average of 3 images taken from 3 sections of each mouse, one-way ANOVA, main effect of antibody shown in legend).
(D) Quantification of TMEM119 mean gray value in the three groups. (n = 3-6 mice/sex/antibody, data shown are an average of 3 images taken from 3 sections of each mouse, one-way ANOVA, p values shown over bars are from Sidak's *post-hoc* test, main effect of antibody shown in legend).
(E) Representative images of $CD68^{Lo}TMEM119^{Hi}$ homeostatic microglia and $CD68^{Hi}TMEM119^{Lo}$ phagocytic microglia.
(F & G) Quantification of $CD68^{Lo}TMEM119^{Hi}$ homeostatic microglia and $CD68^{Hi}TMEM119^{Lo}$ phagocytic microglia in the ACC of the three groups. (n = 3-6 mice/sex/antibody, data shown are a percentage of 12 cells measured per animal across 3 images, one-way ANOVA, p values shown over bars are from Sidak's *post-hoc* test, main effect of antibody shown in legend). All data are mean ± s.e.m. p-values that fall below $p<0.05$ are denoted with an asterisk, and p-values between 0.05 and 0.10 denoted with a #.

277 Fig. 8a). We then stained the brains for Iba1 and RFP to determine whether the microglia after anti-
278 IL34 administration existed pre-surgery (Supp. Fig. 8b). Indeed, we found that >90% of total Iba1+
279 cells were also RFP+ in both control and anti-IL34 treated mice (Supp. Fig. 8c), confirming that the
280 phagocytic cells that arise after treatment were present before antibody injection.

281 As an additional control for our blocking antibody experiments, we next wanted to confirm that the
282 increase in phagocytic microglia was not a result of the remaining microglia simply eating dying or
283 dead microglia. While we did not expect this to be the case given it has been shown that astrocytes,
284 not microglia, are the primary cells that clear microglial debris following low-dose CSF1r-inhibition[28]
285 leading to partial microglia loss, we generated another cohort of mice where we performed ICV
286 injections of either control or anti-IL34 at P15 and collected these mice shortly after at 12 and 24 hours
287 post-surgery. While the ICV injection does not directly induce tissue damage in the ACC, we observed
288 a significant increase in microglia number in control mice 12 hours following surgery when compared
289 to anti-IL34 mice or even control mice at 24- or 48-hours post-surgery (Supp. Fig. 9a, dotted line). We
290 believe that this is likely a proliferation of microglia that occurs acutely after surgery and is caused by
291 either the physical stress of the surgery on the brain or a direct effect of the anesthesia (isoflurane)
292 which has been shown to cause an inflammatory response in aged microglia[29]. Interestingly, we did
293 not see an increase in microglia in anti-IL34 mice 12 hours post-surgery, and we only began to
294 observe a reduction in microglia number from baseline starting 24 hours post-surgery. In addition to
295 microglia number, we assessed phagocytic cups (which are normally virtually non-existent in P17
296 mouse cortex), homeostatic ($CD68^{Lo}/TMEM^{Hi}$) and phagocytic ($CD68^{Hi}/TMEM^{Lo}$) cells, and GFAP
297 fluorescence as a marker of activated astrocytes. We observed an increase in phagocytic cups in anti-
298 IL34 mice primarily at 12, but still at 24 hours post-surgery (Supp. Fig. 9b-c). This corresponded to an
299 increase in phagocytic microglia (Supp. Fig. 9e, g). We did not see an effect of blocking antibody
300 treatment on homeostatic microglia (Supp. Fig. 9d), although we believe there may have been a floor
301 effect given so few of the control-treated microglia met the criteria for “homeostatic” this shortly after
302 surgery. Finally, we observed a significant interaction between post-surgery time and antibody

303 treatment in GFAP mean gray value demonstrating increased GFAP fluorescence in anti-IL34 mice
304 24 hours post-surgery, which is when we observed the initial decrease in microglia numbers and
305 suggests that astrocytes are indeed eating the dead microglia (Supp. Fig. 9f) in support of previous
306 literature[28]. Taken together, we found that our I.C.V. injection surgery causes increased microglial
307 proliferation in control mice 12 hours post-surgery, an effect which is blunted by anti-IL34 injection.
308 Further, anti-IL34 increases phagocytic microglia as early as 12 hours post-surgery, and microglia
309 begin to die 24 hours post-surgery alongside an increase in reactive astrocytes. In sum, we believe
310 that these data provide strong evidence to suggest that the anti-IL34 microglia phenotypes we observe
311 are not simply a consequence of microglial engulfment of other dead microglia immediately after
312 surgery.

313 **IL34 inhibition causes aberrant eating of VGlut2+ thalamocortical synapses.**

314 It is well established that microglia engulf aberrant or unnecessary synapses in neuronal development.
315 This process requires precise regulation to ensure appropriate synapses are eaten, while necessary
316 synapses are maintained[30]. While some signals have been identified that act as “eat me” tags on
317 neurons and synapses destined for destruction[22,31–34], very few “don’t eat me” signals have been
318 discovered that instruct microglia to stop eating to protect structurally mature, functioning circuits[35].
319 Recent work from our lab has shown that microglia in the ACC at P8 exhibit elevated phagocytic
320 capacity, actively engulf VGlut2+ thalamocortical presynaptic material, and stop by P10[16] (Figure 5a).
321 Because this timing coincides with the increase in IL34 we observed between P8 and P15 (Figure 1),
322 and because decreasing IL34 signaling both genetically and with blocking antibodies induces
323 phagocytic, immature microglia (Figures 2 & 4), we hypothesized that IL34 may be acting as a
324 neuronal “brake” on microglial synaptic pruning to protect stable synapses from phagocytic microglia
325 as the circuit matures. To test this, we triple-stained for Iba1, CD68, and VGlut2 and 3D reconstructed
326 individual microglia in IMARIS to quantify the volume of presynaptic (VGlut2) material contained within
327 microglial lysosomes. We found a two-fold increase in the amount of synaptic material contained
328 within microglia from mice treated with anti-IL34 compared to control and anti-CSF1 treated mice

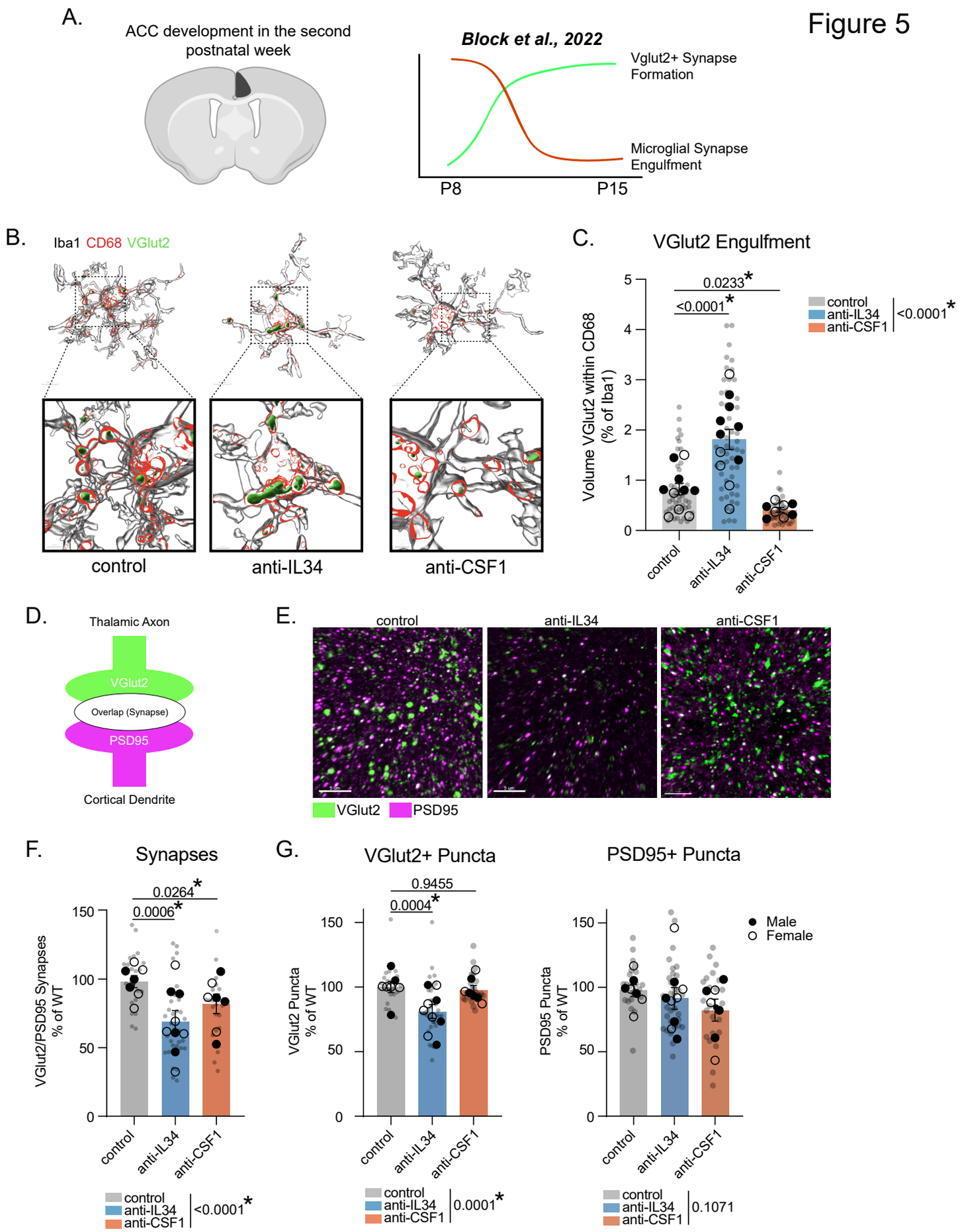

Figure 5. IL34 Inhibition Causes Aberrant Eating of VGlut2+ Synapses.
(A) Representative schematic of previous findings regarding the developmental period of microglia-neuron interactions in the ACC during the second postnatal week. Conceptual diagram constructed based on data from Figure 4 in Block et al., 2022.
(B-C) IMARIS representative images and quantification of VGlut2 synaptic material engulfed in CD68+ lysosomes within microglia in control, anti-IL34, and anti-CSF1 treated mice. (n = 3-5 mice/sex/antibody, 4-6 cells analyzed per mouse, 141 cells total, individual microglia represented by gray circles, animal averages represented by black dots, nested one-way ANOVA, p values shown are from Sidak's *post-hoc* test, main effect of antibody shown in legend).
(D) Thalamocortical synapse numbers in the ACC can be quantified by co-immunostaining for VGlut2 (pre-synaptic marker) and PSD95 (post-synaptic marker) and counting the number of overlapping pre- and post-synaptic puncta.
(E) Representative images of VGlut2 and PSD95 co-staining in control, anti-IL34, or anti-CSF1 brains. Synapses can be identified by the white overlap between the two channels.
(F) Quantification of synapses in control, anti-IL34, and anti-CSF1 treated mice. (n = 3-5 litters/sex/antibody, 3 sections imaged per animal, 1-2 animals per litter, images represented by gray circles, litter averages represented by black dots, nested one-way ANOVA, p values shown are from Sidak's *post-hoc* test, main effect of antibody shown in legend).
(G) Quantification of Vglut2+ puncta and PSD95+ puncta in control, anti-IL34, and anti-CSF1 treated mice. (n = 3-5 litters/sex/antibody, 3 sections imaged per animal, images represented by gray circles, animal averages represented by black dots, nested one-way ANOVA, p values shown are from Sidak's *post-hoc* test, main effect of antibody shown in legend). All data are mean ± s.e.m. All p-values that fall below p<0.05 are denoted with an asterisk.

329 (Figure 5b-c). Interestingly, we also found a significant *decrease* in synaptic material engulfed in the
330 anti-CSF1 mice compared to controls, suggesting that blocking CSF1 has the opposite effect on
331 microglial synaptic engulfment (Figure 5b-c). We also found that anti-IL34 and anti-CSF1 had opposite
332 effects on microglial cell volume (anti-IL34 decreased volume while anti-CSF1 increased cell volume)
333 and on overall phagocytic capacity (Supp. Fig. 7f-g).

334 We next determined if this change in microglial over-engulfment of synapses translated to a change
335 in overall synapse number. To do so, we quantified numbers of VGlut2+ thalamocortical synapses by
336 staining for presynaptic VGlut2 and postsynaptic PSD95 and calculating overlap of the two signals
337 (Figure 5d). When we did this in our mice that received either control, anti-IL34, or anti-CSF1, we
338 found a significant reduction in the number of synapses in mice treated with anti-IL34 and anti-CSF1
339 compared to IgG-treated controls (Figure 5e-f). In the anti-IL34 group this was driven by a reduction
340 in VGlut2+ presynaptic puncta, not PSD95+ postsynaptic puncta (Figure 5g). While surprising that we
341 observed a reduction in synapses in anti-CSF1 mice, we believe this change was driven by a non-
342 microglial mechanism since we observed a *decrease* in engulfment in this group. Taken together,
343 these results provide evidence that IL34 and CSF1 signaling have differential effects on cortical
344 microglia function at P15, and that blocking IL34 increases engulfment of thalamocortical synapses
345 at an inappropriate developmental window, leading to synapse loss.

346 **IL34 overexpression at P1 increases TMEM119 expression and decreases synaptic engulfment**
347 **at P8.**

348 In a final set of experiments, we tested the sufficiency of IL34 signaling to control microglia maturation
349 and synapse pruning in early cortical development. To do this, we took advantage of the fact that IL34
350 is expressed at low levels at P8 (Figure 2 & Supp. Fig. 4) and overexpressed IL34 by injecting an
351 AAV-IL34 (AAV5-hSyn1-eGFP-T2A-mIL34-FLAG-WPRE) or AAV-GFP (AAV5-hSyn1-eGFP-WPRE)
352 control into the PFC of P1 mice (Figure 6a). With this approach we robustly increased IL34 protein
353 expression at P8 in the ACC as evidenced by IL34 ELISA (Figure 6b). We then counted microglia and
354 measured TMEM119 expression within those microglia at P8. While we found no difference in

355 microglia number, we did observe a trending increase in TMEM119 expression in AAV-IL34-FLAG
356 mice compared to control (Figure 6c-e). This is notable, as TMEM119 is not highly expressed in
357 normal cortical microglia until the second postnatal week in mice[3], and thus suggests that
358 overexpressing IL34 before it is endogenously produced at high levels in development is, at least
359 partially, sufficient to accelerate the maturation of microglia. Next, we used IMARIS 3D reconstructions
360 to measure microglial phagocytic capacity and VGlut2 synaptic engulfment. Excitingly, we observed
361 a marked reduction in phagocytic capacity and decreased synaptic engulfment in microglia in AAV-
362 IL34-injected mice (Figure 6f-h). In line with this, we observed a significant increase in microglial
363 ramification measured with sholl analysis (Figure 6i). Finally, we quantified overall synapses and found
364 a significant increase in Vglut2/PSD95 synapses in AAV-IL34 mice, likely a consequence of reduced
365 microglial pruning in these animals (Figure 6j-k). In sum, virally expressing IL34 from P1-P8
366 prematurely increases microglial TMEM119 expression and decreases microglial phagocytic
367 capabilities and synaptic pruning.

368 **Discussion.**

369 It is now increasingly recognized that microglia exhibit a vast array of functional states
370 throughout the developing brain[18,36–38]. Here, we provide evidence that IL34, a neuron-derived
371 cytokine that signals through the CSF1r on microglia, functionally matures cortical microglia in a
372 discrete window of neurodevelopment. We show that IL34 is upregulated in the second week of
373 postnatal life and is expressed at a higher level in active, glutamatergic neurons in the ACC at P10.
374 This developmental increase in IL34 expression in the ACC corresponds to an increase in microglia
375 number, ramification, TMEM119 expression, and a decrease in phagocytic capacity. Genetic KO of
376 IL34 prevents these microglial developmental processes from progressing, and as a result, KO mice
377 have behavioral deficits at both P15 (USVs) and adulthood (EPM). Acute blocking of IL34 at P15
378 increases immature ($TMEM^{Lo}$), phagocytic ($CD68^{Hi}$) microglia, decreases cell ramification and
379 TMEM119 expression, and re-activates microglia to eat thalamocortical synapses during an
380 inappropriate developmental window (P15). In turn, virally overexpressing IL34 in neurons early in

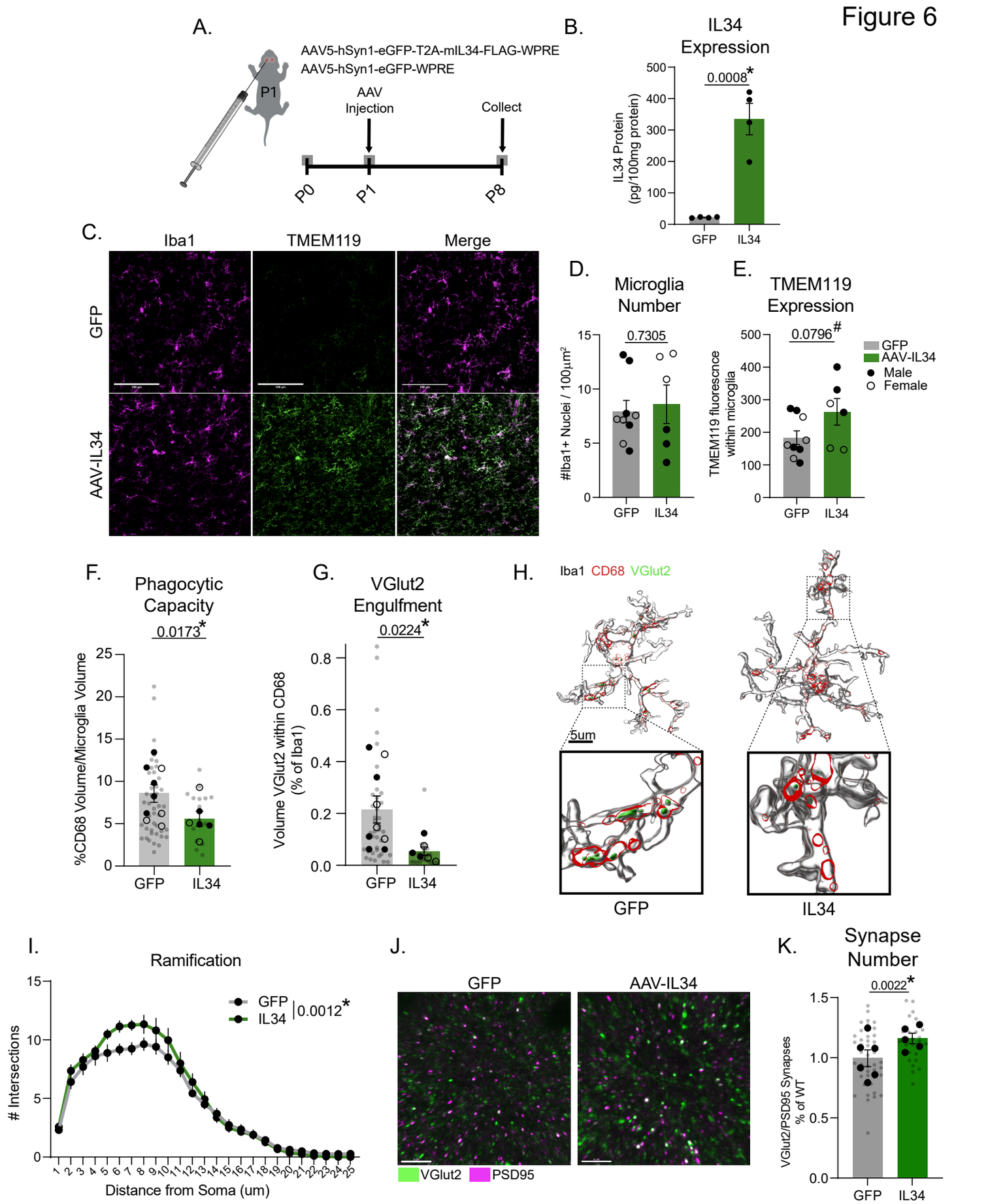

Figure 6. IL34 Viral Overexpression at P1 increases TMEM119 expression and reduces microglial engulfment of synapses
(A) Experimental schematic of P1 viral injections into the prefrontal cortex and tissue collection at P8.
(B) ELISA data validating an increase in IL34 protein in mice injected with the IL34 overexpression virus. (n = 4-5 mice/group, p value shown is from unpaired t-test).
(C) Representative images of Iba1 and TMEM119 co-immunostain in the ACC of mice injected with either control GFP or AAV-IL34. Scale = 100µm.
(D) Quantification of microglia numbers in the two groups. (n = 3-5 mice/sex/virus, data shown are an average of 3 images taken from 3 sections of each mouse, p value shown is from an unpaired t test).
(E) Quantification of TMEM119 mean gray value in the two groups. (n = 3-5 mice/sex/virus, data shown are an average of 3 images taken from 3 sections of each mouse, p value shown is from an unpaired t test).
(F) Quantification of microglia phagocytic capacity in control GFP and AAV-IL34 mice. (n = 3-5 mice/sex/virus, 4-6 cells analyzed per mouse, 58 cells total, individual microglia represented by gray circles, animal averages represented by black dots, p values shown are from nested t-test).
(G) Quantification of VGlut2 synaptic material engulfed in CD68+ lysosomes within microglia in control GFP and AAV-IL34 mice. (n = 3-5 mice/sex/virus, 4-6 cells analyzed per mouse, 58 cells total, individual microglia represented by gray circles, animal averages represented by black dots, p values shown are from nested t-test).
(H) IMARIS representative images of VGlut2 synaptic material engulfed in CD68+ lysosomes within microglia in control GFP and AAV-IL34 mice. Scale = 5µm.
(I) Sholl analysis quantification of microglial process ramification in control GFP and AAV-IL34 mice. (n = 3-5 mice/sex/virus, 4-6 cells analyzed per mouse, two-way ANOVA distance from soma x virus, p values shown are main effect of virus).
(J) Representative images of VGlut2 and PSD95 co-staining in control GFP or AAV-IL34 brains. Synapses can be identified by the white overlap between the two channels.
(K) Quantification of synapses in control GFP and AAV-IL34 mice. (n = 3-4 litters/sex/antibody, 3 sections imaged per animal, 1-2 animals per litter, images represented by gray circles, litter averages represented by black dots, p values shown are from nested t-test).
All data are mean ± s.e.m. All p-values that fall below p<0.05 are denoted with an asterisk, and p-values between 0.05 and 0.10 denoted with a #.

381 development (P8) is sufficient to accelerate microglial functional maturity and inhibit synaptic pruning.
382 These results establish IL34 as a “brake” signal for microglial phagocytosis in the context of synaptic
383 pruning, as well as unveiling its greater role in fine-tuning microglial identity and functional state in
384 development.

385 In our first set of experiments, we found that IL34 expression is higher in Fos+, glutamatergic
386 neurons. Despite these exciting initial findings, follow up work is needed to define its release dynamics
387 from neurons. We were limited with our RNA FISH experiments to assessing mRNA only within the
388 nucleus (DAPI), but there is transcriptomic data suggesting that IL34 mRNA is present at the synapse
389 and may be locally translated there[39]. Additionally, we found that blocking IL34 specifically prevented
390 microglia from engulfing presynaptic (VGlut2+) terminals in the ACC. This does not, however, inform
391 what role it may play in engulfing post-synaptic material, which microglia have been shown to do[40], or
392 other neuronal components such as spines or cell bodies in other brain regions. As a secreted protein,
393 it is unlikely that IL34 is tagging individual synapses for engulfment like complement[22]. Thus, based
394 on our data, we believe that IL34 has a broad effect on local microglia once the circuit has stabilized.
395 The discovery that IL34 gene expression is lower in GABAergic neurons compared to glutamatergic
396 neurons at postnatal day 10 was not unsurprising to us. While the timing of putative inhibitory synaptic
397 pruning in the ACC is not well described, GABAergic pruning generally occurs later in development
398 than excitatory synaptic pruning[41], in part due to the delayed maturation of GABA circuits as the GABA
399 switch happens in the second postnatal week[42]. It stands to reason that GABAergic neurons may
400 upregulate IL34 expression directly following their circuit maturation, and this should be addressed in
401 future work.

402 While both IL34 and CSF1 bind to the same receptor on microglia, our findings demonstrate
403 that they have distinct effects on microglial functional differentiation, with separate roles in
404 development. Prior to our work, *Kana et al.*, demonstrated that microglia in culture treated with IL34
405 vs. CSF1 have different transcriptional responses, but no data existed that tested the role of these
406 two molecules on microglia function in an intact, developing brain[14,43]. It has been shown that IL34

407 binding to CSF1r in macrophages leads to increased phosphorylation of downstream targets in the
408 MAPK pathway such as p38a, while CSF1-binding preferentially phosphorylates members of the
409 STAT and ribosomal S6K pathways[44], which may provide one explanation for their differential effects
410 on cell function. Additionally, *Boulakirba et al.,* have shown that IL34 polarizes macrophages to a less
411 "activated" state, by increasing IL-10 and decreasing phagocytosis *in vitro*[45]. It has also been shown
412 that microglia in the gray matter are sensitive to IL34 blocking or ablation, while microglia in the white
413 matter, cerebellum, and brainstem are sensitive to CSF1 blocking or ablation[12,13]. This is consistent
414 with the finding that white matter microglia exhibit different functional and transcriptomic properties
415 compared to gray matter microglia[46,47].Our experiments demonstrate that IL34 signaling is critical not
416 only for gray matter microglial survival and proliferation at these early stages of life, but also for
417 dictating the proper functional development of these cells.

418 Interestingly, we found that microglia number and TMEM119 immunoreactivity in the cortical
419 microglia from IL34 KO mice were indistinguishable from WT cerebellar microglia, suggesting CSF1
420 is capable of maintaining a subset of microglia in the cortex when the primary signal (IL34) is lost[5,11].
421 The question remains, however, whether two distinct populations of microglia are maintained solely
422 by IL34 or CSF1 in the intact brain. This is unlikely given that CSF1 is still expressed, albeit at low
423 levels, in the forebrain of wild type mice[13]. Thus, we hypothesize that IL34/CSF1 functional regulation
424 exists along a spectrum – where the balance of total IL34 vs. CSF1 present in the system can tip cells
425 back and forth between various states. This establishes a novel and exciting framework and suggests
426 that IL34/CSF1 signaling can differentially modulate microglial function across various developmental
427 and disease states and warrants future studies that interrogate the potential role for IL34 signaling in
428 diseases where microglia play a causal role.

429 We observed an unexpected decrease in synapses in the anti-CSF1 mice, despite a decrease
430 in microglial engulfment of pre-synaptic structures compared to control-treated mice (Figure 5). This
431 suggests that CSF1 may be important in other aspects of synaptic development. We believe that our
432 anti-CSF1 manipulation may be directly impacting neurons, since there is some evidence that neurons

433 also express the CSF1 receptor and that signaling through this receptor is protective[48], however we
434 did not rigorously test this hypothesis. There are other reports, however, that also suggest CSF1 can
435 be produced by neurons, but only in the context of stress[49], injury[50], or ethanol withdrawal[51], and that
436 this upregulation has negative consequences for neurons and synaptic transmission. These findings
437 are in line with our observations that blocking CSF1 decreased microglial engulfment of synapses,
438 and suggest that indeed, CSF1 may be primarily involved in maintaining immature phagocytic
439 microglia. In sum, more work will need to be done to tease out the precise effects of CSF1 and IL34
440 signaling in different cell types in different contexts, but overall, our data demonstrate a need for
441 greater attention to and interpretation of results utilizing CSF1r inhibitors. It also sets a precedent for
442 modeling different microglial functional states in *in vitro* models using different growth factors (CSF1
443 vs. IL34) and demands additional scrutiny of these models for replicating an intact brain environment
444 (with homeostatic levels of these cytokines across contexts)[52].

445 To summarize, our results unveil a novel mechanism by which neurons communicate with
446 microglia to control their function in postnatal development. In addition to promoting survival, IL34
447 signaling to microglia acts as an important cue that matures microglia and prevents over-eating of
448 thalamocortical synapses. These data shed light on the functional relevance of IL34, making it a
449 unique and interesting target for future studies of microglia and neurons.

450 **Acknowledgements**

451 This work was supported by funding from the NIH (1F31NS130757-01) and the Cure
452 Alzheimer's fund to B.A.D and S.D.B. We would like to thank D. Saban for the IL34$^{LacZ/LacZ}$ mice, R.
453 Weimer from Genentech for the IL34 and CSF1 function-blocking antibodies, M. Alter for his
454 continuous and invaluable discussion of the work, and the Duke Light Microscopy Core facility for
455 microscope and image analysis support.

456 **Author Contributions**

457 S.D.B and A.M.C conceived the study and, together with B.A.D, designed the experiments.
458 B.A.D, D.M.N, G.G., M.J.C, M.D., A.S., S.A., and A.F. performed experiments; D.R. and A.S. provided

critical reagents, B.A.D analyzed all data and wrote the manuscript together with S.D.B, who oversaw the project.

Declaration of Interests

The authors declare no competing interests.

Inclusion and Diversity

We support inclusive, diverse, and equitable conduct of research.

Key resources table

REAGENT or RESOURCE	SOURCE	IDENTIFIER
Antibodies		
Guinea pig anti-VGlut2 1:2000	Synaptic Systems	Cat#135404; RRID: AB_887884
Chicken anti-IBA1 1:1000	Synaptic Systems	Cat# 234 009, RRID:AB_2891282
Rat anti-CD68 1:1000	Biolegend	Cat# 137001 (also 137002), RRID:AB_2044003
Chicken anti-Beta Galactosidase (LacZ) 1:1000	Aves Labs	Cat# BGL1010, RRID:AB_2313508
Guinea pig anti-TMEM119 1:1000	Synaptic Systems	Cat# 400 004, RRID:AB_2744645
Rabbit anti-PSD95 1:250	Thermo Fisher Scientific	Cat# 51-6900, RRID:AB_2533914
Rabbit anti-c-Fos 1:1000	Millipore	Cat# ABE457, RRID:AB_2631318
Rabbit anti-P2y12 1:2000	Anaspec	Cat#AS-55043A: RRID: AB_2298886
Rabbit anti-Sox9 1:2000	Millipore	Cat# AB5535, RRID:AB_2239761
Mouse anti-Olig2 1:2000	Millipore	Cat#MABN50; RRID: AB_10807410
Guinea pig anti-Neun	Synaptic Systems	Cat# 266 004, RRID:AB_2619988
Rabbit anti-RFP	Rockland	Cat# 600-401-379, RRID:AB_2209751
Anti-gp120 ragweed control blocking antibody	Easley-Neal et al., 2019	Genentech (Gift)
Anti-IL34 blocking antibody	Easley-Neal et al., 2019	Genentech (Gift)
Anti-CSF1 blocking antibody	Easley-Neal et al., 2019	Genentech (Gift)
Bacterial and virus strains		
AAV8-hSyn1-hM3D(Gq)-mCherry	Bryan Roth (Unpublished)	Addgene Cat#50474
AAV8-hSyn1-EGFP	Bryan Roth (Unpublished)	Addgene Cat#50475
AAV5-hSyn1-eGFP-T2A-mIL34-FLAG-WPRE	Anne Schaefer (Unpublished)	
AAV5-hSyn1-eGFP-WPRE	Anne Schaefer (Unpublished)	
Biological samples		
Chemicals, peptides, and recombinant proteins		
TRIzol Reagent	Thermo Fisher Scientific	Cat#15596026
DAPI	Thermo Fisher Scientific	Cat#D1306
Fluoromount-G	Thermo Fisher Scientific	Cat#00-4959-52
Deschloroclozapine (DCZ)	Tocris	Cat#7193

Vectashield PLUS Antifade Mounting Medium w/ DAPI	Vector Laboratories	Cat# H-2000-10
4-hydroxytamoxifen (4OHT)	Sigma-Aldrich	Cat#H6278
Cell Lysis Buffer 2	RND Systems	895347
Chloroform	Sigma-Aldrich	Cat#C2432
Normal Goat Serum	VWR	Cat#102038-610
Triton X-100 Surfact-Amps	Thermo Fisher Scientific	Cat#28314
Tris-buffered Saline (TBS)	Thermo Fisher Scientific	Cat#28358
2-Propanol	Sigma-Aldrich	Cat#I9516
Qiagen QuantiTect Reverse Transcription kit	Qiagen	205311
Critical commercial assays		
IL34 ELISA	RND Systems	Cat#M3400
RNAScope	ACD Bio	RNAScope Multiplex Fluorescent V1 Assay
HCR RNAFISH	Molecular Instruments	HCR RNA-FISH Bundle with custom probes for Gad2, Fos, and IL34
Bradford Protein Assay	BioRad	Cat#5000111
Deposited data		
Experimental models: Cell lines		
Experimental models: Organisms/strains		
WT Mice (C57BL/6J)	Jackson Labs	Cat#000664
IL34 KO Mice	Dr. Daniel Saban (Gift)	Greter et al., 2012
P2Y12CreER mice	INIA Consortium (Gift), Jackson Labs	Cat#034727
Ai14 Mice	Jackson Labs	Cat#007914
Oligonucleotides		
qPCR *IL34*: Forward	Harvard Primer Bank ID: 18921437a1	TTGCTGTAAACA AAGCCCCAT
qPCR *IL34*: Reverse	Harvard Primer Bank ID: 18921437a1	CCGAGACAAAGG GTACACATTT
qPCR *CSF1*: Forward	Harvard Primer Bank ID: 192801a1	ATGAGCAGGAGT ATTGCCAAGG
qPCR *CSF1*: Reverse	Harvard Primer Bank ID: 192801a1	TCCATTCCCAAT CATGTGGCTA
qPCR *18s*: Forward	This paper	GAATAATGGAATA GGACCGC
qPCR *18s*: Reverse	This paper	CTTTCGCTCTGGT CCGTCTT
Recombinant DNA		
Software and algorithms		
Ethovision	Noldus Technology	RRID:SCR_000441; https://www.noldus.com/ethovision-xt

Prism 9.0.0	GraphPad Software, Inc.	RRID:SCR_002798; https://www.graphpad.com
MUPET v2.1	Van Segbroeck et al., 2017	https://github.com/mvansegbroeck/mupet
FV31S-SW	Olympus Corporation	https://www.olympus-lifescience.com/en/support/downloads/
Imaris 9.5.1	Oxford Instruments	RRID:SCR_007370; https://imaris.oxinst.com/
Python 2019.3.3	Python Programming Language	RRID:SCR_008394; http://www.python.org/
Ilastik	Berg et al., 2019	RRID:SCR_015246; http://ilastik.org/
Avisoft-Ultrasound Gate recording software	Avisoft Bioacoustics	RRID:SCR_014436; http://www.avisoft.com/downloads/
MatlabR_2022a	Mathworks	RRID:SCR_001622; https://www.mathworks.com/
ImageJ	NIH	RRID:SCR_003070; https://imagej.nih.gov/ij/
Other		

STAR Methods.

Animals.

All procedures relating to animal care and treatment conformed to Duke Institutional Animal Care and Use Committee and National Institutes of Health guidelines (protocol no. A107-19-05 and renewal no. A062-22-03). Animals were group housed in a standard 12:12-hour light–dark cycle. The C57BL/6J mouse line was obtained from Jackson Laboratory, stock no. 000664. The IL34$^{LacZ/LacZ}$ mice were a gift from Dr. Daniel Saban at Duke University and were originally generated by Dr. Marco Colonna[11]. Ai14 tdtomato fl/fl mice were ordered as breeder females from Jackson Laboratory, stock no. 007914 and B6(129S6)-P2ry12em1(icre/ERT2)Tda/J (P2yr12$^{CreER/+}$) mice were recently restored from cryopreservation by the INIA (International Narcotics Interdiction Association) consortium and were gifted to S.D.B. These mice are now available from Jackson Laboratory, stock no. 034727.

qPCR.

For the qPCR time course, wild-type mice were sacrificed and saline perfused at the six described ages (P7, P14, P21, P30, P38, P55) and their brains flash-frozen in 2-methylbutane in dry ice and stored at -80C. Tissue punches were taken from the anterior cingulate cortex, nucleus accumbens, amygdala, and cerebellum and stored in 500µL TRIzol (ThermoFisher, 15596026). RNA was extracted from the tissue using TRIzol based chloroform extraction, followed by isopropanol precipitation. Resulting RNA concentration was measured using a NanoDrop spectrophotometer (ND-1000) and either 200 ng or 1000 ng (depending on starting concentration) of RNA were reverse transcribed into cDNA using a Qiagen QuantiTect Reverse Transcription kit (205311). qPCR was performed on an Eppendorf Realplex ep Mastercycler using Sybr/Rox amplification with a QuantiFAST PCR kit (204056). Primer sequences are listed in Supplementary Table 1. All samples were loaded in triplicate and all plates were run on the same day to ensure comparability across plates. Fold change was calculated using the $2^{-\Delta\Delta CT}$ method with 18S as an endogenous control for sample normalization.

IL34 ELISA.

For all ELISA tissue collection, mice were anaesthetized with CO_2 and transcardially perfused with ice-cold saline prior to brain collection. For tissue punches, brains were flash-frozen in dry ice and embedded in O.C.T. (Sakura Finetek) and stored at -80C. Tissue was sectioned on the Leica CM50 cryostat until brain region of interest was visible, then brain region was punched using a 1mm RapidCore tissue punch (Ted Pella) and frozen at -80C. Prior to the tissue-punch ELISA, tissue was homogenized in 300µL 1X PBS using the Dremel Tissue-Tearor (BioSpec, 985370-04). Then, 300µL Cell Lysis Buffer 2 was added to the samples (R&D Biosystems, 895347) and they were placed on an orbital shaker at 200rpm for 30 minutes before spinning down in a 4°C centrifuge at 13,200 rpm for 20 minutes. Samples were stored at -20C overnight or -80C long term. All samples were run according to the manufacturer's instructions for the kit (R&D Biosystems, M3400). All protein was normalized to total protein in the sample using a standard bradford assay kit (BioRad, DC™ Protein Assay Kit, 5000111), which was assessed the same day as the ELISA. The equation used to calculate pg/100mg protein is: (IL34 concentration (pg/mL) *100) / (total protein (mg/mL) *1000).

Microglia Staining.

For all immunohistochemistry experiments, mice were perfused with ice-cold saline followed by 4% paraformaldehyde (PFA). Tissue was then post-fixed in 4% PFA for 24 hours prior to cryoprotection in 30% sucrose with 0.1% sodium azide. Brains were flash-frozen in 2-methylbutane in dry ice and stored at -80C until sectioned. Sections were collected at 40µM and kept free-floating at -20C in

512 cryoprotectant until stained. Free-floating sections were washed 3X in 1X PBS prior to blocking in a
513 10% normal goat serum (NGS) solution with 0.3% Triton-X in 1X PBS for 1 hour. Sections were
514 incubated in primary antibodies overnight at 4°C. The primary antibodies used were Chicken anti-
515 Iba1 (Synaptic Systems, 234 009, 1:1000), Guinea Pig anti-TMEM119 (Synaptic Systems, 400 004,
516 1:1000), Rat anti-CD68 (Biolegend, 137002, 1:1000). The following day, sections were washed 3X in
517 1X PBS and incubated in secondary antibodies for 2 hours at room temperature prior to mounting on
518 gelatin-subbed slides and cover-slipping with Vectashield plus DAPI (Vector Labs, H-2000-10).
519
520 **Microglia Imaging and Analysis.**
521 Images of microglial Iba1, TMEM119, and CD68 staining were acquired on a Zeiss AxioImager M2 at
522 20X magnification. 19 Z-Stacks at a 1μM step size were acquired and maximum intensity projections
523 were used for all analyses. For *Microglia Cell Counting*, single channel, maximum intensity, Iba1
524 images were counted using the supervised machine learning tool Ilastik[53] with the Pixel + Object
525 Segmentation pipeline. All automatic counts were validated by blinded hand counts. Object
526 segmentation outputs were then combined and analyzed using custom python scripts. For *Microglial*
527 *TMEM119 expression,* first, an Iba1 mask was generated using Ilastik's pixel segmentation pipeline
528 on single channel Iba1 images. This mask was used to control for any mean gray value differences
529 that may be a result of decreased cell number or process complexity. Following mask generation,
530 TMEM119 mean gray value within the Iba1 mask was calculated using a custom Fiji script. All details
531 and code for these analyses can be found at github.com/bendevlin18/mgla_img_analysis_pipeline.
532 Finally, for *Microglia 2D Sholl Analysis*, using the Iba1 stain, individual microglia were selected for
533 analysis from each image by an individual blind to sex, genotype, and age. Those individual microglia
534 were put through the Ilastik pixel segmentation pipeline to generate binary segmentations of the
535 images. These binary segmentations were processed using a custom python script based on the sholl
536 analysis fiji plugin that skeletonizes the image and plots concentric rings from the soma of each cell,
537 measuring the intersections of those rings with cell processes. All code for 2D sholl analysis is also
538 available on GitHub. https://github.com/bendevlin18/sholl-analysis-python.
539
540 **Microglia Phagocytic Capacity Imaging and Analysis**
541 For microglia phagocytic capacity, microglia (Iba1) and CD68 staining was imaged using a Leica SP8
542 upright confocal. Individual microglia were imaged at a 63X magnification with a Z-stack step size of
543 0.33 μM. These images were then imported into IMARIS (Oxford Instruments, v9.0) and surfaces
544 rendered of the Iba1 and CD68 channels to generate 3D reconstructions of the microglia and their
545 lysosomes. The phagocytic capacity calculation was as follows: (total CD68 volume within microglia /
546 total microglial volume (Iba1)) *100.
547
548 **Microglia Heterogeneity Quantification.**
549 To quantify microglial heterogeneity, representative microglia were selected by a blind experimenter
550 from every image using the Iba1 channel. Each cell was selected using the freehand selection tool in
551 Fiji (ImageJ) and TMEM119 and CD68 mean gray value were measured within each selection. 4 cells
552 were measured per 20X images, and 3 images were analyzed per animal. TMEM119 and CD68
553 measurements were then normalized to Iba1 expression and histograms representing the distribution
554 of expression values were plotted to determine value cutoffs for high, low, and mid expressing cells
555 of each marker (supp. Fig. 7b-c). Individual cells were assigned high, low, or mid based on these
556 cutoffs, and percentages of cells (out of 12 total) falling into each category were calculated per animal.
557 The entire python script used for this analysis is available on GitHub.
558 https://github.com/bendevlin18/microglia_tmem_cd68_heterogeneity.
559

560 **Neuron, Astrocyte, Oligodendrocyte Stain and Quantification**
561 Free-floating sections were washed 3X in 1X PBS prior to blocking in a 10% normal goat serum (NGS)
562 solution with 0.3% Triton-X in 1X PBS for 1 hour. Sections were incubated in primary antibodies
563 overnight at 4°C. The primary antibodies used were Rabbit anti-Sox9 (Millipore, AB5535, 1:1000),
564 Guinea Pig anti-Neun (Synaptic Systems, 266 004, 1:1000), Mouse anti-Olig2 (Millipore, MABN50,
565 1:250). The following day, sections were washed 3X in 1X PBS and incubated in secondary antibodies
566 (1:200) for 2 hours at room temperature prior to mounting on gelatin-subbed slides and cover-slipping
567 with Vectashield plus DAPI (Vector Labs, H-2000-10). To quantify overall numbers of neurons,
568 astrocytes, and oligodendrocytes in the cortex and braitem, images were acquired on a Zeiss
569 AxioImager M2 at 20X magnification. 19 Z-Stacks at a 1μM step size were taken and maximum
570 intensity projections were used for all analyses. Single channel, maximum intensity, images of each
571 of the three stains were counted using Ilastik with the Pixel + Object Segmentation pipeline. All
572 automatic counts were validated by blinded hand counts. Object segmentation outputs were then
573 combined and analyzed using custom python scripts.
574
575 **Synaptic Staining.**
576 Samples were collected and processed as described above. Free-floating sections were rinsed in 1X
577 TBST (0.2% Triton X-100) 3 times for 10 minutes prior to block. Sections were then incubated in 5%
578 NGS in 1X TBST for 1 hour at room temperature. Sections were then incubated in primary antibody
579 diluted in 5% NGS in 1X TBST overnight at 4°C. The primary antibodies used were Guinea Pig anti-
580 VGlut2 (Synaptic Systems, 135 404, 1:2000), Rabbit anti-PSD95 (ThermoFisher, 51-6900, 1:350) for
581 overall synapse counts, or Guinea Pig anti-VGlut2 (Synaptic Systems, 135 404, 1:2000), Rat anti-
582 CD68 (Biolegend, 137002, 1:1000), and Chicken anti-Iba1 (Synaptic Systems, 234 009, 1:500).
583 Following primary incubation, sections were washed 3X for 10 minutes in TBS and then incubated in
584 secondary antibody diluted in 5% NGS in 1X TBST for 2 hours at room temperature. Sections were
585 mounted on gelatin-subbed slides and cover-slipped with Fluoromount G (ThermoFisher, 00-4959-
586 52).
587
588 **Synaptic Imaging and Analysis.**
589 Synapse images were acquired on an Olympus FV3000 inverted confocal. Images were taken at 60X
590 magnification with a 1.6X optical zoom. A 4x4 tile scan with 4, 0.33 μM step Z-stacks were obtained.
591 Synapse images were analyzed using SynBot[54]. Synapses were identified by the colocalization of
592 pre- (Vglut2) and post- (PSD95) synaptic puncta.
593
594 **Synaptic Engulfment Imaging and Analysis.**
595 Synaptic Engulfment images were acquired on an Olympus FV3000 inverted confocal. Images were
596 taken at 60X magnification with a 2.3X optical zoom. A 2x2 tile scan with 100-110, 0.33 μM step Z-
597 stacks were obtained. Whole, stitched image stacks were imported into IMARIS (Oxford Instruments,
598 v9.0) and microglial surfaces were rendered using the Iba1 channel. Individual microglia were selected
599 and reconstructed (up to 3/image) and used to mask the CD68 channel. A surface was created from
600 each Iba1-masked CD68 channel and the CD68 surface was used to mask the VGlut2 channel.
601 Surfaces were created of the CD68-masked VGlut2 signal and volumes of all surfaces were exported
602 for analysis. The phagocytic capacity was calculated as described above. The volume of synaptic
603 material engulfed was normalized to Iba1 cell volume.
604
605 **Behavior.**
606 *Ultrasonic Vocalizations.*

We performed ultrasonic vocalization testing as previously described[25]. Briefly, pups were removed from their cage and individually placed in a cotton-lined cup within a sound-attenuating chamber under an Avisoft Condenser ultrasound microphone (Avisoft Bioacoustics CM16/CMPA). suspended four inches above the contained pup. The dam and any remaining littermates were removed from the testing room in the home cage. After 3 min of recording, pups were weighed and sexed before being returned to their home cage. After the dam attended to each returned pup, the home cage was returned to the colony room. Analysis of USV .wav files was done using the MATLAB (MatlabR_2022a) machine-learning program MUPET to quantify the number of calls, the energy of the calls, and all syllable information. Forty-unit syllable repertoires were generated for each dataset and manually inspected before USV similarity was calculated and heatmaps were generated.

Open Field.

Adult mice (P50-55) were placed in a 50 cm × 50 cm square enclosure with 38-cm-high walls and allowed to explore freely for 10 minutes. Behaviors (distance moved and velocity) were recorded and analyzed using EthoVision video tracking software (Noldus). Center avoidance was assessed by comparing time spent at the periphery of the chamber to time spent in the center (middle third of chamber).

Social Preference.

Adult mice (P60-65) were assessed for social preference using a three-chambered preference test. On test day, subject and stimulus animals were habituated to the testing room for a minimum of for 1 h before testing. Each mouse was then tested for the preference to investigate a novel object (rubber duck) versus a novel social stimulus (age and sex-matched stimulus animal). Mice were placed in the middle chamber with the rubber duck confined in a clear plexiglass cylindrical cage on one side of the test and the novel conspecific confined in an identical cage on the other side for 10 minutes. The test was recorded with a Logitech webcam, and all behavior was manually quantified using Solomon Coder by an observer blind to sex and treatment. The social preference score was calculated as: (time spent investigating social stimulus / total time spent investigating either stimulus) * 100.

Elevated Plus Maze.

Male and Female adult mice (P70-75) were tested individually in the elevated plus maze (each arm 10cm wide by 52 cm long) to measure anxiety-like behavior. On the day of testing, mice were habituated to the testing room for at least 1 hour prior to start. Males and females were tested on separate days. One by one, each mouse was placed in the center of the elevated plus maze and their movement throughout the maze was tracked for 5 minutes. Behaviors were recorded and analyzed using Ethovision (Noldus), and the endpoints measured are as follows: Distance Moved, Velocity, Time in Open Arms, Time in Closed Arms, Time in Center, # of Transitions from Open to Closed Arms. The “Percent in Open Arms” metric was calculated by (time in open arms / time in closed arms) *100.

Barnes Maze.

Male adult mice (P80-90) were tested for memory/cognitive flexibility on Barnes maze over a 5-day period. In the first 3 days, each mouse was placed in the center of a large (45cm, radius) circular platform and given 4 minutes to find and enter the target hole (1 of 20 holes with an escape hatch). This was repeated a total of 3 times for each mouse on each of the first 3 days (Training Phase), and the amount of time taken to find the target hole drastically decreased across the 3 days, indicating that the mice had learned the location of the target hole. On the fourth day, the target hole was moved to another quadrant of the maze, and the mice were tested for 3 trials on day 4 and 5 to measure their reversal learning potential. Ethovision (Noldus) was used to track their performance in this task, and the endpoints analyzed were Time to Escape, Total Nose poke Errors, Time Spent in Original Target Quadrant (reversal only).

P1 Viral Injections

655 Postnatal day 1 mouse pups were placed in a 15mL conical tube and anesthetized in an ice bath for
656 10 minutes. Once pups were unresponsive via toe pinch, they were removed from the conical tube
657 and placed on an ice pack for the duration of the injections. Mice were injected with a glass pulled
658 needle pre-filled with virus connected to a microinjector (KD Scientific, 788100). 200nL was injected
659 over a 30 second period into each hemisphere, and prefrontal cortex was targeted by injecting 2mm
660 posterior to the inferior cerebral vein and 1mm lateral to the sagittal sinus. For the *DREADDs*
661 experiments, we injected one of the following viruses: AAV8-hSyn-hM3D(Gq)-mCherry (Addgene,
662 50474-AAV8), AAV8- hSyn-hM4D(Gi)-mCherry (Addgene, 50475-AAV8), or AAV8-hSyn-EGFP
663 (Addgene, 50465). For the *IL34 Overexpression* experiments, we injected one of the following custom-
664 made viruses: AAV5-hSYN1-eGFP-WPRE (control) or AAV5-hSYN-eGFP-T2A-mIL34-FLAG-WPRE
665 (IL34 overexpressing).
666
667 **P15 and Adult Stereotaxic Injections**
668 Mice were anesthetized using 4% isoflurane pretreated with Ketophen anesthetic (5mg/kg, S.C.), and
669 fitted into a Kopf stereotaxic apparatus for the duration of the surgery. The fur on the head was shaved
670 and, following betadine and ethanol preparation of the skin, a single incision was made. The surface
671 of the skull was cleaned and Bregma was identified. For the *P15 blocking antibody* experiments, all
672 blocking antibodies were obtained from Genentech[12], stored at 4°C and diluted to a working stock of
673 10mg/mL in sterile saline on the day of surgery. A 10uL 1701RN Hamilton syringe (Thomas Scientific,
674 1207K95) with attached pulled glass needle was loaded with 4μL of antibody and lowered into each
675 ventricle (-.7AP, 1ML, 2.4DV to bregma). 2μL were diffused over 2 minutes into each ventricle. For
676 the *adult DREADD* experiments, holes were drilled in the skull over the prefrontal cortex (1.1AP,
677 0.7ML, 2DV to bregma) and 1μL of virus, either AAV8-hSyn-hM3D(Gq)-mCherry (Addgene, 50474-
678 AAV8), or AAV8-hSyn-EGFP (Addgene, 50465), was diffused over 5 minutes in each hemisphere.
679
680 **DREADD DCZ Injections**
681 DCZ (Tocris, 7193) was dissolved in 1% DMSO in sterile saline at a working dilution of 0.05 mg/mL.
682 For the neonatal (P8-10) DREADD DCZ injections, mice were weighed daily prior to injection and
683 injected with a 1mg/kg dose of DCZ at the same time each day (11a.m.). For the adult DREADD DCZ
684 injections, mice were weighed and injected 15 minutes apart to allow for collection 90 minutes post
685 DCZ administration.
686
687 **RNA In Situ Staining, Imaging, and Analysis**
688 *RNAScope*
689 Brains for RNAScope were collected 2 hours following the final DCZ injection at P10. The mice were
690 deeply anesthetized using Avertin (tribromoethanol) and transcardially perfused with ice-cold saline
691 and their brains embedded in O.C.T. (Sakura Finetek) and flash frozen in dry ice. The brains were
692 sectioned at 20uM thickness and thaw mounted onto Superfrost Plus slides (Fisher Scientific, 12-550-
693 15). Slides were stored at -80C until stained. We performed RNAScope (ACDBio) in accordance with
694 the manufacturer's protocol. Briefly, tissue was fixed for 15 minutes in 4% PFA followed by gradual
695 dehydration for 5 minutes each in 50%, 70% and 100% EtOH solutions. The samples were then
696 treated with protease for 30 minutes, briefly washed, and then incubated with primary probes for 2
697 hours at 37°C. The primary probes used were C1-Gad2, C2-VGlut1, and C3-IL34. Following
698 hybridization, the tissue went through a series of 4 amplification steps per kit instructions. After the
699 fourth amplification, the tissue was washed, and coverslipped with Vectashield plus DAPI (Vector
700 Labs, H-2000-10). Slides were stained in batches of 4 and imaged within 72 hours of the staining on
701 a Leica SP8 upright confocal. 19 step Z-Stack images at a thickness of 0.33μM of the ACC were taken
702 with the 40X objective. 3 sections per animal were imaged and included in the analysis.

703 *HCR RNAFish*
704 Brains for HCR RNAFish (Molecular Instruments) were collected and sectioned and pretreated
705 (fixation and dehydration) in the same manner as RNAScope. Following fixation and dehydration, the
706 tissue was placed in primary probe solution overnight at 37°C. The primary probes used were B1-
707 Gad2, B2-Fos, and B3-IL34. The next day, tissue was washed at 37°C in increasing concentrations
708 of 5X SSCT buffer and then incubated with hairpins directed against the primary probes overnight at
709 37°C. On the final day, the tissue was washed in 100% 5X SSCT and cover slipped using
710 Fluoromount G (ThermoFisher, 00-4959-52). Imaging of these samples was performed using an
711 Olympus Fluoview 3000 inverted confocal with the 30X objective on the same settings as the
712 RNAScope imaging.
713 *Analysis*
714 Images from RNAScope and RNAFish pipelines were analyzed in IMARIS (Oxford Instruments,
715 v9.0) using the "Imaris for Cell Biologists" plugin to generate cells from the DAPI stain and to count
716 each RNAScope puncta as a separate "vesicle" type within that cell. The volume of the DAPI stain
717 was included in the output as well as the number of each vesicle type. Every cell in the image was
718 included in the analysis and cells were determined to be "glutamatergic" or "GABAergic" based on a
719 threshold adjusted number of Vglut1 puncta vs. Gad2 puncta. Additionally, cells were determined to
720 be Fos+ or Fos- based on an average of 6 puncta adjusted for cell size. IL34 puncta number was
721 normalized to total DAPI volume and averaged for all cells of a given type within a given animal. The
722 code used to process the data is publicly available at
723 https://github.com/bendevlin18/RNA_in_situ_single_cell_quant.git.
724
725 **Statistics.**
726 Statistical tests were performed using GraphPad Prism 9. Raw data as well as a description of the
727 tests and results (including multiple comparison corrections and post-hoc analyses) are provided. In
728 all experiments, both male and female mice were included at sufficient power (n ≥ 3 biological
729 replicates) and statistics were first run including sex as a variable (e.g. three-way ANOVA with sex x
730 age x genotype). In all cases where there was not a main effect of sex, male and female mice were
731 then combined for subsequent statistical testing. Unless otherwise noted, data are mean ± S.E.M.

732 **References.**

733 1. Paolicelli, R. C. *et al.* Microglia states and nomenclature: A field at its crossroads. *Neuron* **110**, 3458–3483 (2022).

734 2. Matcovitch-Natan, O. *et al.* Microglia development follows a stepwise program to regulate brain homeostasis.

735 *Science* **353**, (2016).

736 3. Bennett, M. L. *et al.* New tools for studying microglia in the mouse and human CNS. *Proc. Natl. Acad. Sci.* **113**,

737 E1738–E1746 (2016).

738 4. Bennett, F. C. *et al.* A Combination of Ontogeny and CNS Environment Establishes Microglial Identity. *Neuron* **98**,

739 1170-1183.e8 (2018).

740 5. Nandi, S. *et al.* The CSF-1 receptor ligands IL-34 and CSF-1 exhibit distinct developmental brain expression patterns

741 and regulate neural progenitor cell maintenance and maturation. *Dev. Biol.* **367**, 100–113 (2012).

742 6. Stanley, E. R. & Chitu, V. CSF-1 Receptor Signaling in Myeloid Cells. *Cold Spring Harb. Perspect. Biol.* **6**, a021857

743 (2014).

744 7. Chitu, V., Gokhan, Ş., Nandi, S., Mehler, M. F. & Stanley, E. R. Emerging Roles for CSF-1 Receptor and its Ligands in

745 the Nervous System. *Trends Neurosci.* **39**, 378–393 (2016).

746 8. Elmore, M. R. P. *et al.* CSF1 receptor signaling is necessary for microglia viability, which unmasks a cell that rapidly

747 repopulates the microglia-depleted adult brain. *Neuron* **82**, 380–397 (2014).

748 9. Erblich, B., Zhu, L., Etgen, A. M., Dobrenis, K. & Pollard, J. W. Absence of Colony Stimulation Factor-1 Receptor

749 Results in Loss of Microglia, Disrupted Brain Development and Olfactory Deficits. *PLOS ONE* **6**, e26317 (2011).

750 10. Wang, Y. *et al.* IL-34 is a tissue-restricted ligand of CSF1R required for the development of Langerhans cells and

751 microglia. *Nat. Immunol.* **13**, 753–760 (2012).

752 11. Greter, M. *et al.* Stroma-Derived Interleukin-34 Controls the Development and Maintenance of Langerhans

753 Cells and the Maintenance of Microglia. *Immunity* **37**, 1050–1060 (2012).

754 12. Easley-Neal, C., Foreman, O., Sharma, N., Zarrin, A. A. & Weimer, R. M. CSF1R Ligands IL-34 and CSF1 Are

755 Differentially Required for Microglia Development and Maintenance in White and Gray Matter Brain Regions. *Front.*

756 *Immunol.* **10**, (2019).

757 13. Badimon, A. *et al.* Negative feedback control of neuronal activity by microglia. *Nature* **586**, 417–423 (2020).

758 14. Kana, V. *et al.* CSF-1 controls cerebellar microglia and is required for motor function and social interaction. *J.*
759 *Exp. Med.* **216**, 2265–2281 (2019).
760 15. Semple, B. D., Blomgren, K., Gimlin, K., Ferriero, D. M. & Noble-Haeusslein, L. J. Brain development in rodents
761 and humans: Identifying benchmarks of maturation and vulnerability to injury across species. *Prog. Neurobiol.* **106–**
762 **107**, 1–16 (2013).
763 16. Block, C. L. *et al.* Prenatal environmental stressors impair postnatal microglia function and adult behavior in
764 males. *Cell Rep.* **40**, 111161 (2022).
765 17. Zhan, L. *et al.* Proximal recolonization by self-renewing microglia re-establishes microglial homeostasis in the
766 adult mouse brain. *PLOS Biol.* **17**, e3000134 (2019).
767 18. Li, Q. *et al.* Developmental Heterogeneity of Microglia and Brain Myeloid Cells Revealed by Deep Single-Cell
768 RNA Sequencing. *Neuron* **101**, 207-223.e10 (2019).
769 19. Hanamsagar, R. *et al.* Generation of a microglial developmental index in mice and in humans reveals a sex
770 difference in maturation and immune reactivity. *Glia* **65**, 1504–1520 (2017).
771 20. Huang, Y. *et al.* Microglia use TAM receptors to detect and engulf amyloid β plaques. *Nat. Immunol.* **22**, 586–
772 594 (2021).
773 21. Litvinchuk, A. *et al.* Complement C3aR Inactivation Attenuates Tau Pathology and Reverses an Immune
774 Network Deregulated in Tauopathy Models and Alzheimer's Disease. *Neuron* **100**, 1337-1353.e5 (2018).
775 22. Schafer, D. P. *et al.* Microglia Sculpt Postnatal Neural Circuits in an Activity and Complement-Dependent
776 Manner. *Neuron* **74**, 691–705 (2012).
777 23. Harry, G. J. & Kraft, A. D. Microglia in the developing brain: A potential target with lifetime effects.
778 *NeuroToxicology* **33**, 191–206 (2012).
779 24. De Biase, L. M. *et al.* Local Cues Establish and Maintain Region-Specific Phenotypes of Basal Ganglia Microglia.
780 *Neuron* **95**, 341-356.e6 (2017).
781 25. Ceasrine, A. M. *et al.* Maternal diet disrupts the placenta–brain axis in a sex-specific manner. *Nat. Metab.* 1–14
782 (2022) doi:10.1038/s42255-022-00693-8.
783 26. Segbroeck, M. V., Knoll, A. T., Levitt, P. & Narayanan, S. MUPET—Mouse Ultrasonic Profile ExTraction: A Signal
784 Processing Tool for Rapid and Unsupervised Analysis of Ultrasonic Vocalizations. *Neuron* **94**, 465-485.e5 (2017).

785 27. Hwang, H. M. & Hashimoto-Torii, K. Activation of the anterior cingulate cortex ameliorates anxiety in a
786 preclinical model of fetal alcohol spectrum disorders. *Transl. Psychiatry* **12**, 1–9 (2022).
787 28. Zhou, T. *et al.* Microglial debris is cleared by astrocytes via C4b-facilitated phagocytosis and degraded via
788 RUBICON-dependent noncanonical autophagy in mice. *Nat. Commun.* **13**, 6233 (2022).
789 29. Wang, Z. *et al.* Critical role of NLRP3-caspase-1 pathway in age-dependent isoflurane-induced microglial
790 inflammatory response and cognitive impairment. *J. Neuroinflammation* **15**, 109 (2018).
791 30. Paolicelli, R. C. *et al.* Synaptic Pruning by Microglia Is Necessary for Normal Brain Development. *Science* **333**,
792 1456–1458 (2011).
793 31. Cheadle, L. *et al.* Sensory Experience Engages Microglia to Shape Neural Connectivity through a Non-
794 Phagocytic Mechanism. *Neuron* **108**, 451-468.e9 (2020).
795 32. Gunner, G. *et al.* Sensory lesioning induces microglial synapse elimination via ADAM10 and fractalkine
796 signaling. *Nat. Neurosci.* **22**, 1075–1088 (2019).
797 33. Filipello, F. *et al.* The Microglial Innate Immune Receptor TREM2 Is Required for Synapse Elimination and
798 Normal Brain Connectivity. *Immunity* **48**, 979-991.e8 (2018).
799 34. Jiang, D. *et al.* Neuronal signal-regulatory protein alpha drives microglial phagocytosis by limiting microglial
800 interaction with CD47 in the retina. *Immunity* **55**, 2318-2335.e7 (2022).
801 35. Lehrman, E. K. *et al.* CD47 Protects Synapses from Excess Microglia-Mediated Pruning during Development.
802 *Neuron* **100**, 120-134.e6 (2018).
803 36. Hammond, T. R. *et al.* Single-Cell RNA Sequencing of Microglia throughout the Mouse Lifespan and in the
804 Injured Brain Reveals Complex Cell-State Changes. *Immunity* **50**, 253-271.e6 (2019).
805 37. Masuda, T. *et al.* Spatial and temporal heterogeneity of mouse and human microglia at single-cell resolution.
806 *Nature* **566**, 388–392 (2019).
807 38. Grabert, K. *et al.* Microglial brain region−dependent diversity and selective regional sensitivities to aging. *Nat.*
808 *Neurosci.* **19**, 504–516 (2016).
809 39. Ouwenga, R. *et al.* Transcriptomic Analysis of Ribosome-Bound mRNA in Cortical Neurites In Vivo. *J. Neurosci.*
810 **37**, 8688–8705 (2017).

811 40. Dayananda, K. K. *et al.* Early life stress impairs synaptic pruning in the developing hippocampus. *Brain. Behav.*
812 *Immun.* **107**, 16–31 (2023).
813 41. Favuzzi, E. *et al.* GABA-receptive microglia selectively sculpt developing inhibitory circuits. *Cell* **184**, 4048-
814 4063.e32 (2021).
815 42. Furukawa, M. *et al.* Neonatal maternal separation delays the GABA excitatory-to-inhibitory functional switch
816 by inhibiting KCC2 expression. *Biochem. Biophys. Res. Commun.* **493**, 1243–1249 (2017).
817 43. Nakamichi, Y., Udagawa, N. & Takahashi, N. IL-34 and CSF-1: similarities and differences. *J. Bone Miner. Metab.*
818 **31**, 486–495 (2013).
819 44. Chihara, T. *et al.* IL-34 and M-CSF share the receptor Fms but are not identical in biological activity and signal
820 activation. *Cell Death Differ.* **17**, 1917–1927 (2010).
821 45. Boulakirba, S. *et al.* IL-34 and CSF-1 display an equivalent macrophage differentiation ability but a different
822 polarization potential. *Sci. Rep.* **8**, 256 (2018).
823 46. Safaiyan, S. *et al.* White matter aging drives microglial diversity. *Neuron* **109**, 1100-1117.e10 (2021).
824 47. Ayata, P. *et al.* Epigenetic regulation of brain region-specific microglia clearance activity. *Nat. Neurosci.* **21**,
825 1049–1060 (2018).
826 48. Luo, J. *et al.* Colony-stimulating factor 1 receptor (CSF1R) signaling in injured neurons facilitates protection and
827 survival. *J. Exp. Med.* **210**, 157–172 (2013).
828 49. Wohleb, E. S., Terwilliger, R., Duman, C. H. & Duman, R. S. Stress-Induced Neuronal Colony Stimulating Factor 1
829 Provokes Microglia-Mediated Neuronal Remodeling and Depressive-like Behavior. *Biol. Psychiatry* **83**, 38–49 (2018).
830 50. Guan, Z. *et al.* Injured sensory neuron–derived CSF1 induces microglial proliferation and DAP12-dependent
831 pain. *Nat. Neurosci.* **19**, 94–101 (2016).
832 51. Patel, R. R. *et al.* Ethanol withdrawal-induced adaptations in prefrontal corticotropin releasing factor receptor
833 1-expressing neurons regulate anxiety and conditioned rewarding effects of ethanol. *Mol. Psychiatry* **27**, 3441–3451
834 (2022).
835 52. Schafer, S. T. *et al.* An in vivo neuroimmune organoid model to study human microglia phenotypes. *Cell* **186**,
836 2111-2126.e20 (2023).
837 53. Berg, S. *et al.* ilastik: interactive machine learning for (bio)image analysis. *Nat. Methods* **16**, 1226–1232 (2019).

838 54. Savage, J. T., Ramirez, J., Risher, W. C., Irala, D. & Eroglu, C. SynBot: An open-source image analysis software
839 for automated quantification of synapses. 2023.06.26.546578 Preprint at
840 https://doi.org/10.1101/2023.06.26.546578 (2023).
841

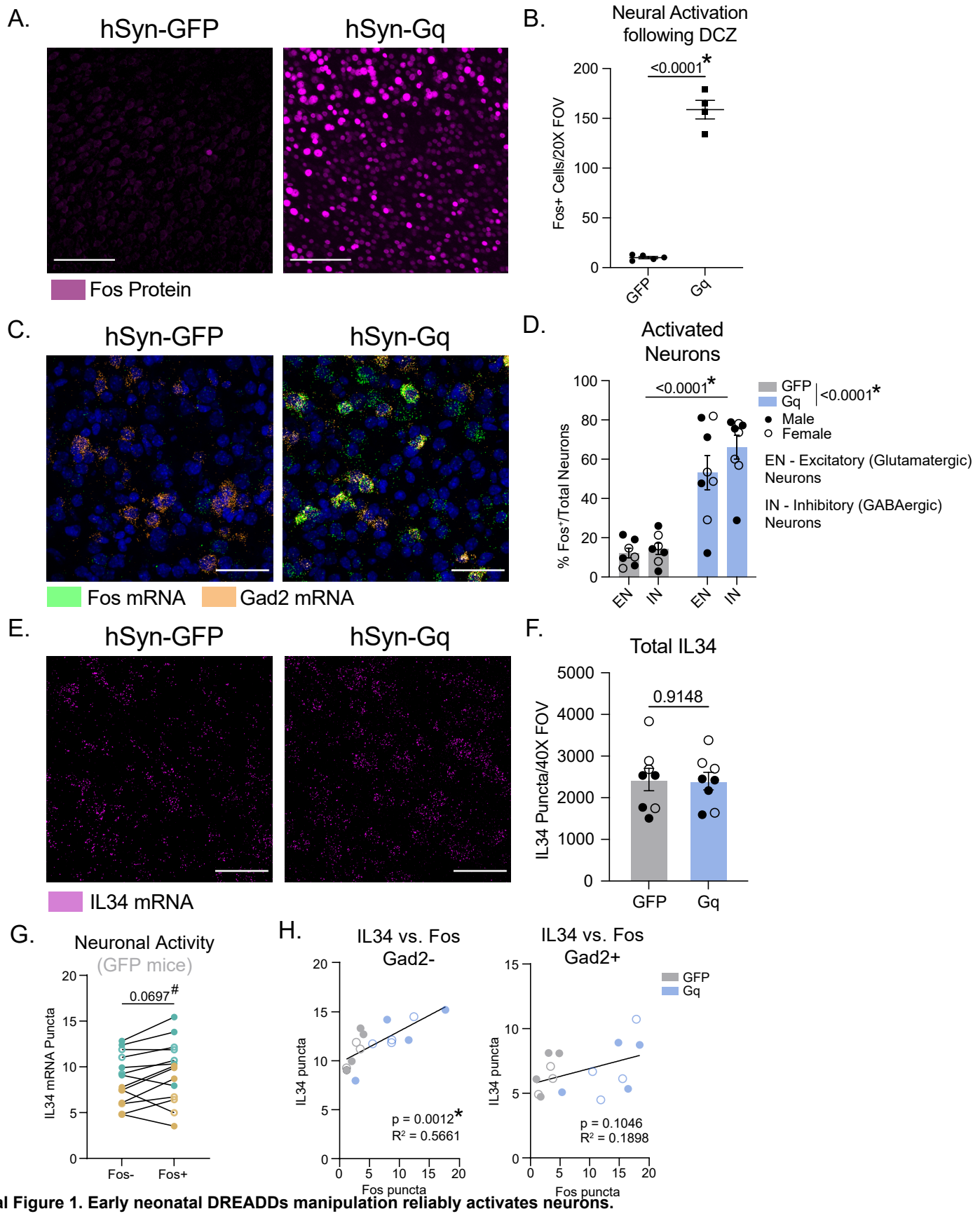

Supplemental Figure 1. Early neonatal DREADDs manipulation reliably activates neurons.
(A-B) Representative images and quantification of Fos+ protein in GFP-injected control mice and Gq-injected excitatory DREADD mice. (n = 4-5 mice/virus, p value shown is from an unpaired t-test). Scale = 100uM
(C-D) Representative images and quantification of Fos+ mRNA in excitatory and inhibitory neurons in GFP and Gq mice. (n=3-4 mice/sex/virus, data shown are an average of 3 images taken from 3 sections of each mouse, one-way ANOVA, main effect of virus shown in legend). Scale = 50uM
(E-F) Total IL34 puncta per 40X field of view in GFP control and Gq mice. (n=3-4 mice/sex/virus, data shown are an average of 3 images taken from 3 sections of each mouse, p value shown is from an unpaired t-test). Scale = 50uM
(G) Quantification of IL34 mRNA puncta in Fos- and Fos+ cells in mice that received the Gq virus. (n = 3-4 mice/sex, data shown are a per animal average of the expression level of all neurons of that type (excitatory vs. inhibitory, and active vs. inactive, total of 5,722 cells analyzed), p value shown is from a paired t-test).
(H) Correlation between IL34 puncta and Fos puncta in mice GFP control and Gq mice separated by neuron subtype. (n = 3-4 mice/sex/virus, data shown is a per animal average of IL34 and Fos puncta in all neurons, p value shown is from a pearson correlation). All data are mean ± s.e.m. p-values that fall below p<0.05 are denoted with an asterisk.

Supp. Figure 1

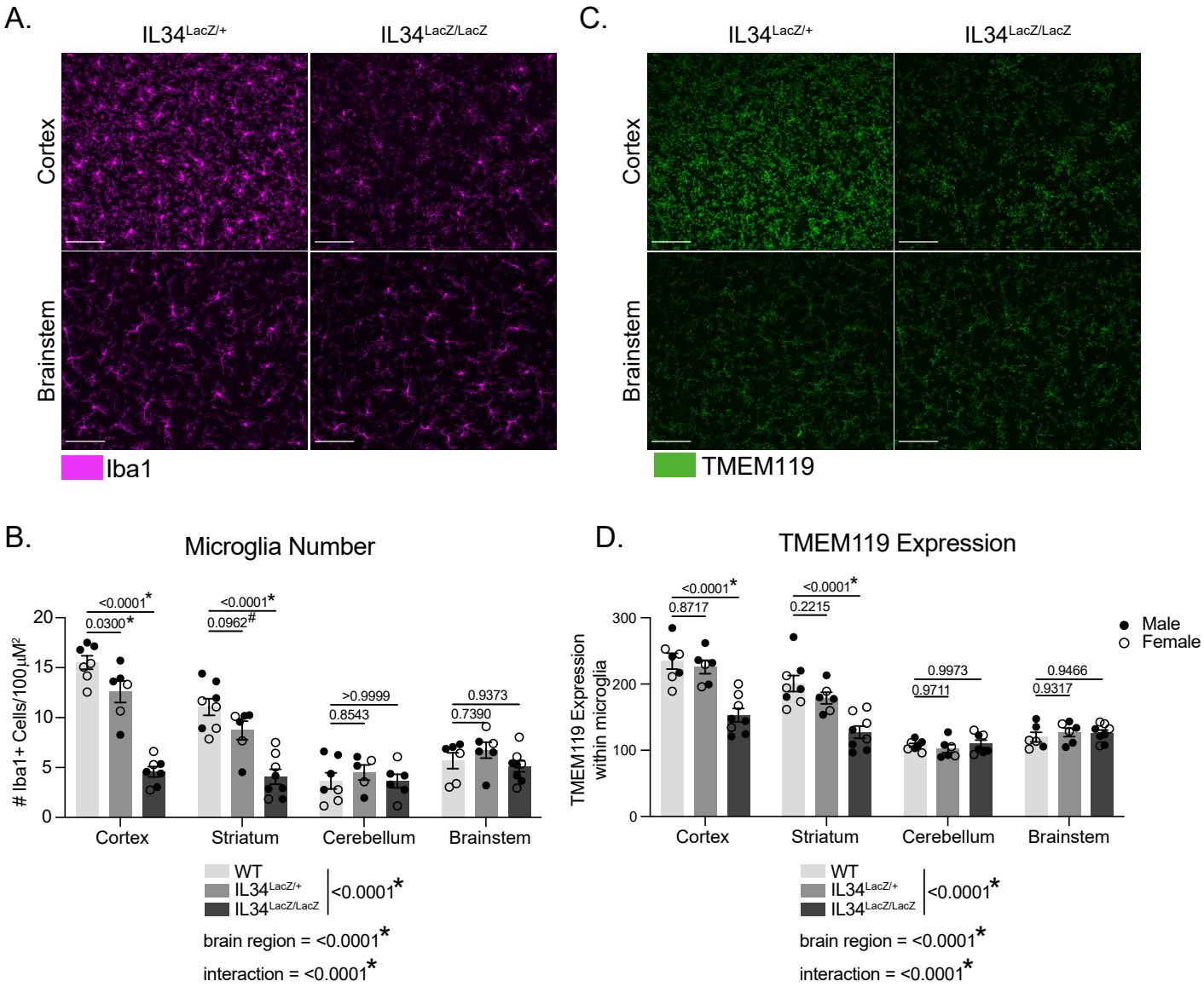

Supplemental Figure 2. IL34 KO impacts microglia numbers and TMEM119 expression in adult cortex and striatum, but not cerebellum or brainstem

(A & C) Representative images of Iba1 stain in WT, IL34$^{LacZ/+}$ and IL34$^{LacZ/LacZ}$ mice from both the cortex and brainstem.

(B & D) Quantification of microglia number and TMEM119 mean gray value in the cortex, striatum, cerebellum, and brainstem from WT, IL34$^{LacZ/+}$,and IL34$^{LacZ/LacZ}$ mice. (n = 2-4 mice/sex/genotype, data shown are an average of three images taken from 3 sections of each mouse, two-way ANOVA, p values shown are from Sidak's *post-hoc* test, main effect of genotype and brain region and interaction effect shown in legend). Scale bar = 100µM. All data are mean ± s.e.m. p-values that fall below p<0.05 are denoted with an asterisk, and p-values between 0.05 and 0.10 denoted with a #.

Kana et al., 2019 - Forebrain Isolated Microglia Bulk RNA-Seq

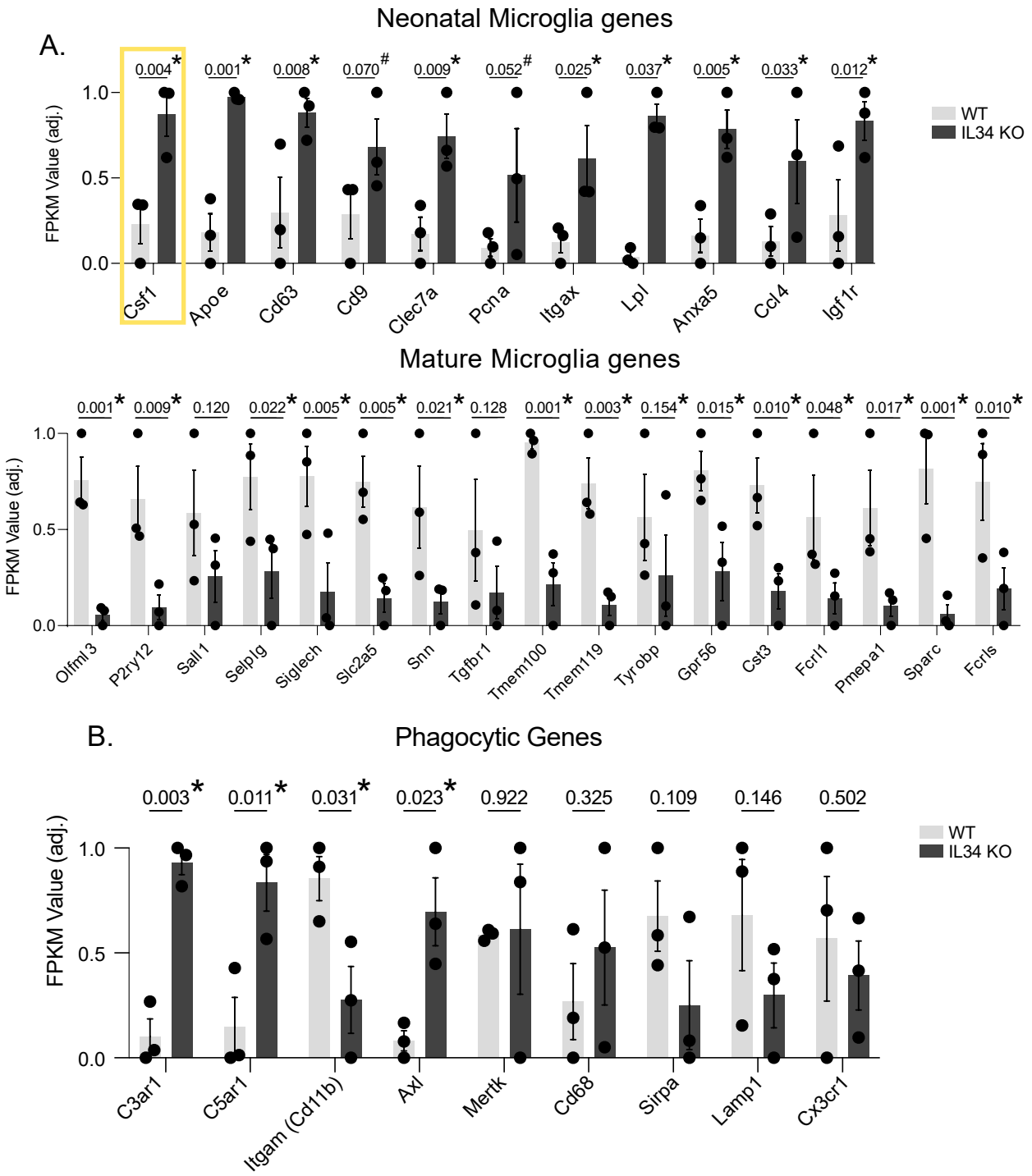

Supplemental Figure 3. IL34 KO impacts microglial transcriptional maturation and dysregulates phagocytic gene expression.

(A) Scaled gene expression (FPKM) of embryonic/neonatal and adult microglia markers from the Forebrain microglia from WT and IL34$^{LacZ/LacZ}$ (IL34 KO) male mice. P values shown are from multiple t-tests function in Graphpad Prism. List of marker genes compiled from sequencing done in Bennett et al., 2016, Matcovitch-Natan 2014, and Li et al., 2019.

(B) Adjusted FPKM gene expression values of candidate phagocytic microglia genes from forebrain microglia from WT and IL34 KO male mice.

P All data are mean ± s.e.m. p-values that fall below $p<0.05$ are denoted with an asterisk and p-values between 0.05 and 0.10 denoted with a #.

Data from this figure was originally generated and published in Kana et al., 2019 and is accessible at GSE133362.

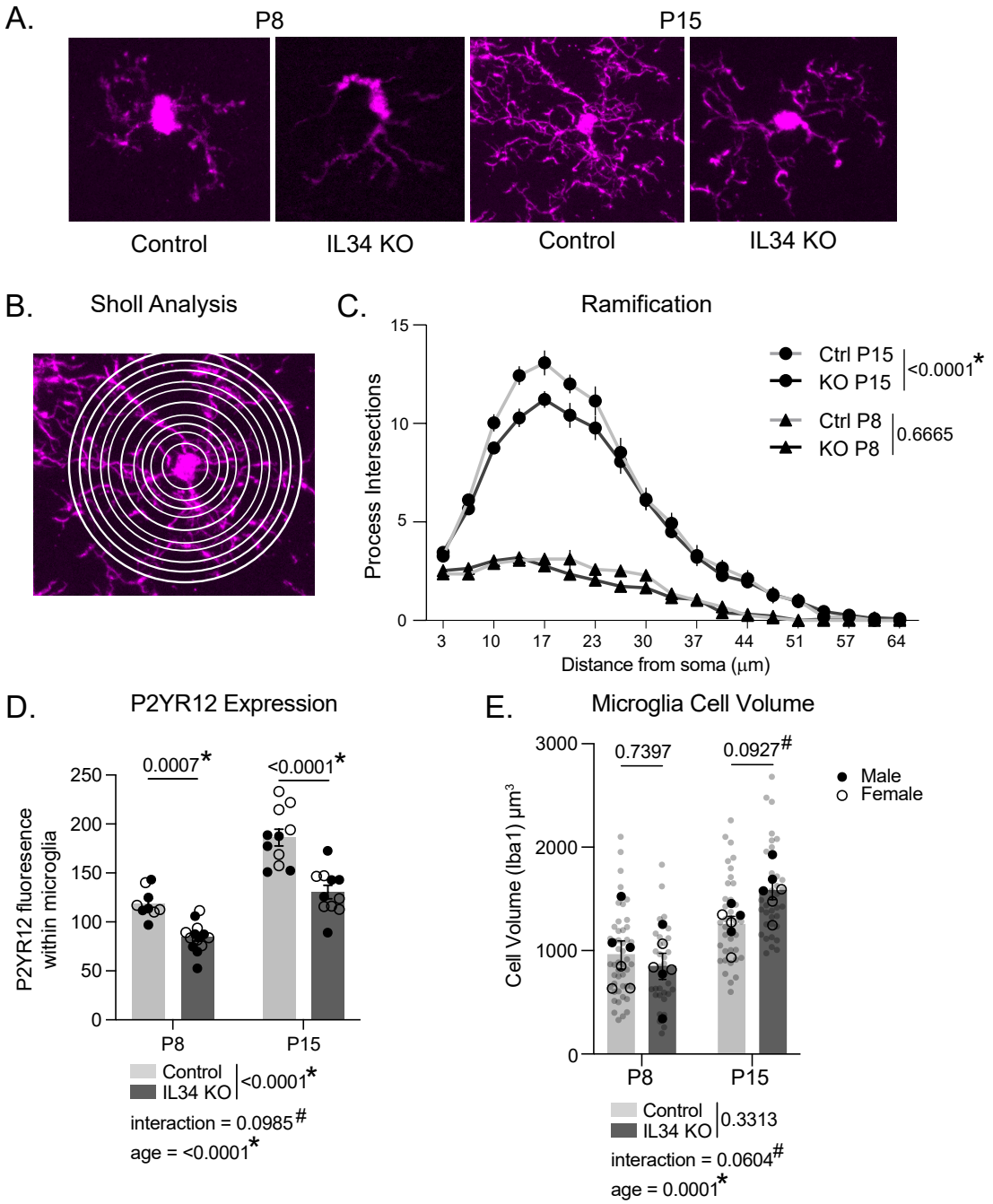

Supplemental Figure 4. IL34 KO impacts microglial ramification, P2YR12 expression, and cell volume at P8 and P15.
(A) Representative images of individual microglia (Iba1 stain) from the anterior cingulate cortex of P8 and P15 Control and IL34 KO mice.
(B-C) Quantification of microglial ramification using sholl analysis (branchpoint intersections with concentric rings of increasing diameter. (n = 5-8 mice/sex/age/genotype, 6 cells analyzed per mouse, two-way ANOVA distance from soma x genotype, p values shown are main effect of genotype).
(D) Quantification of P2YR12 mean gray value in the ACC of P8 and P15 IL34 KO and Control mice (n = 5-8 mice/sex/age/genotype, data shown are an average of 3 images taken from 3 sections of each mouse, two-way ANOVA age x genotype, p values shown over bars are from Sidak's *post-hoc* test, main effect of genotype and age and interaction term shown in legend).
(E) Quantification of microglia Iba1 cell volume from IMARIS 3D reconstructions. (n = 3 mice/sex/age/genotype, 4-6 cells analyzed per mouse, individual microglia represented by gray circles, animal averages represented by black dots, p values shown over bars are from nested t tests). All data are mean ± s.e.m. p-values that fall below p<0.05 are denoted with an asterisk, and p-values between 0.05 and 0.10 denoted with a #.

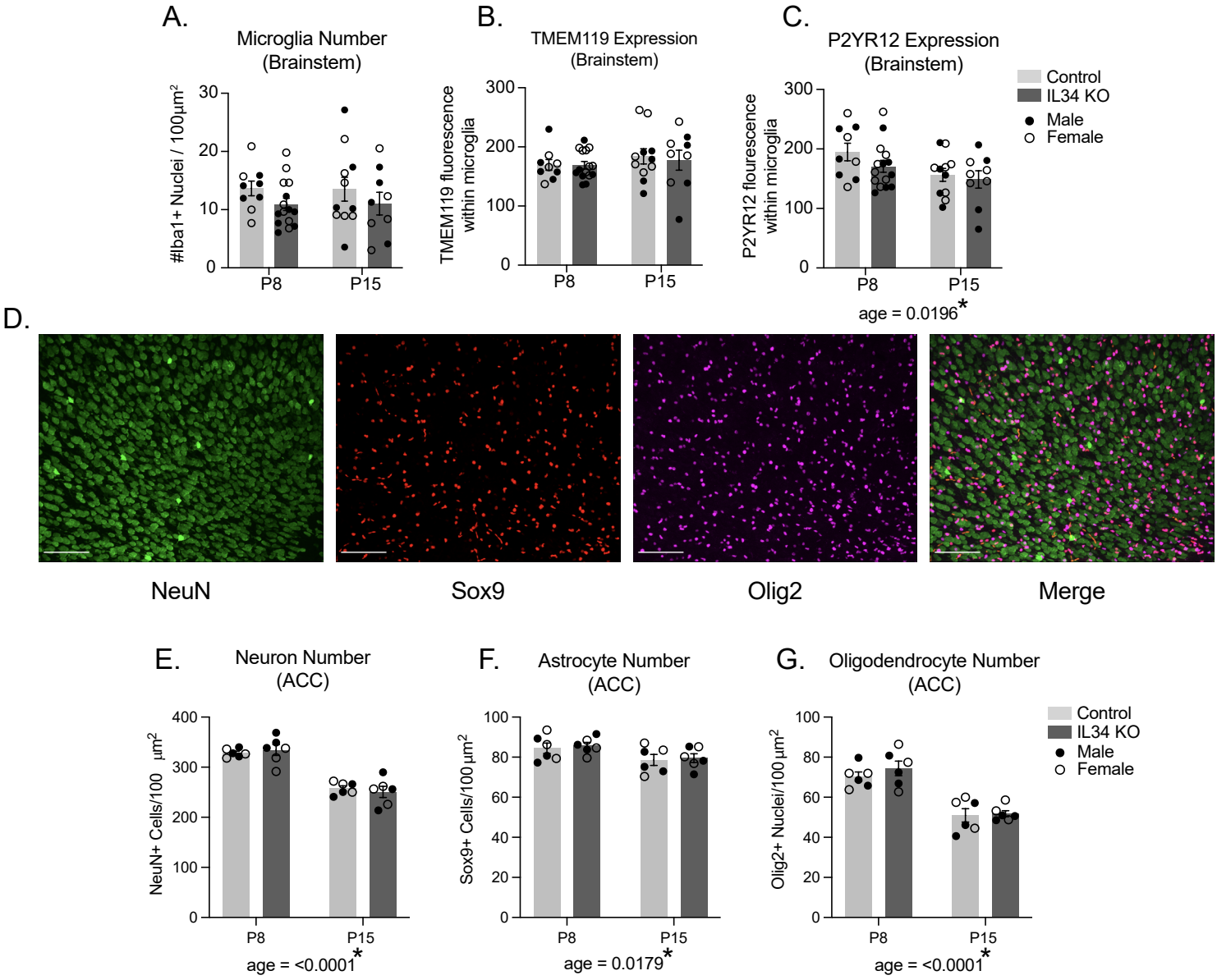

Supplemental Figure 5. IL34 KO does not impact microglia in the brainstem or neurons, astrocytes, or oligodendrocytes in the ACC.
(A-C) Quantification of microglia cell number, TMEM119 expression, and P2YR12 expression from the brainstem of P8 and P15 Control and IL34 KO mice. (n = 5-8 mice/sex/age/genotype, data shown are an average of 3 images taken from 3 sections of each mouse, two-way ANOVA age x genotype).
(D) Representative Image of NeuN, Sox9, Olig2 triple stain for quantification of neuron, astrocyte, and oligodendrocyte numbers/density.
(E-G) Quantification of Neuron, Astrocyte, and Oligodendrocyte numbers in ACC and Brainstem of P8 and P15 Control and IL34 KO mice. (n=3 mice/sex/age/genotype, data shown are an average of 3 images taken from 3 sections of each mouse, two-way ANOVA age x genotype, main effect of age and interaction term shown in legend where significant).
Scale bar = 100µM. All data are mean ± s.e.m. p-values that fall below $p<0.05$ are denoted with an asterisk.

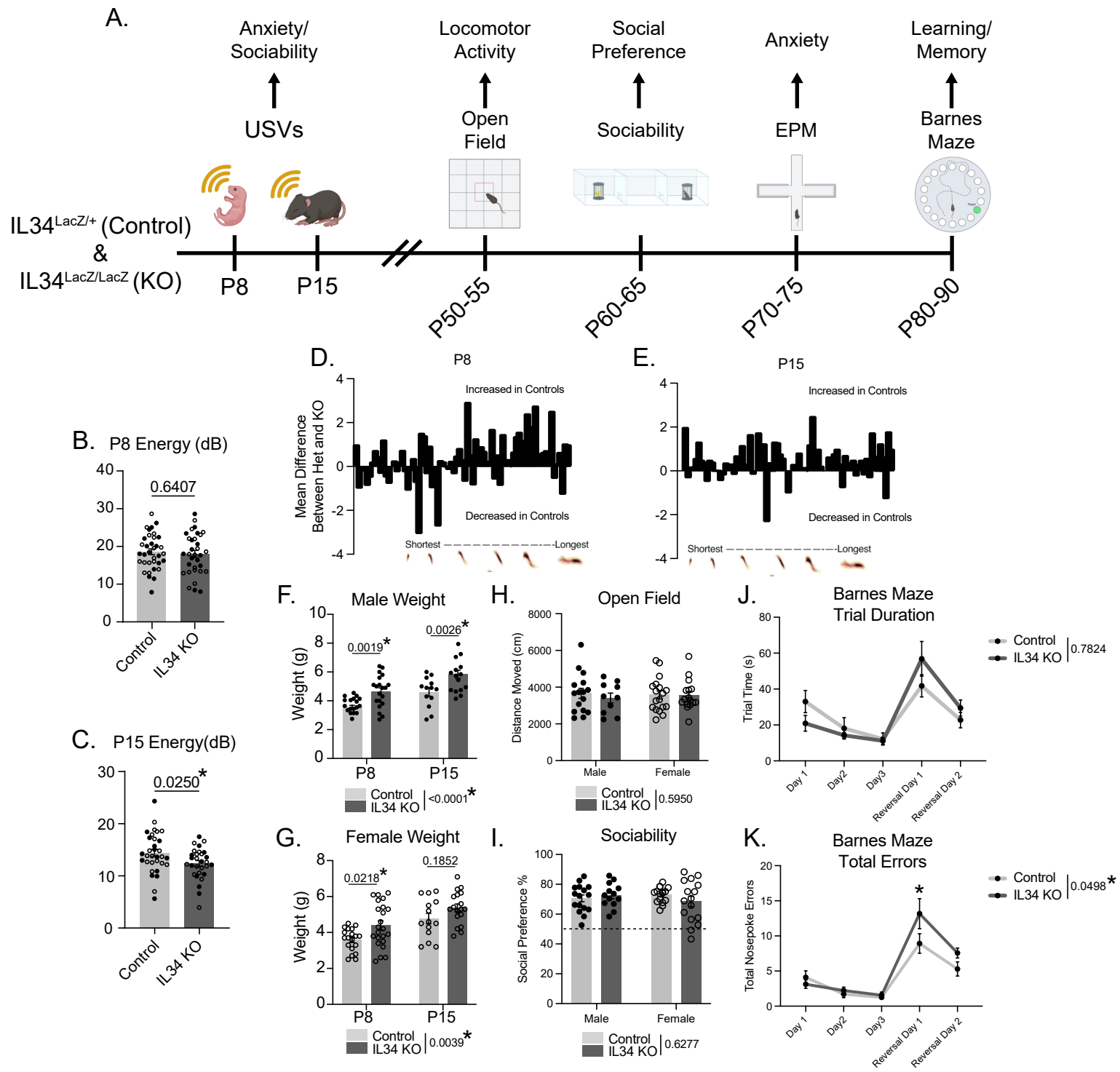

Supplemental Figure 6. IL34 KO impacts developmental weights and adult barnes maze reversal, but does not impact distance moved in the open field or adult sociability

(A) Experimental timeline for IL34 KO behavioral phenotyping in development and adulthood.
(B-C) Quantification of USV call energy differences between control and IL34 KO mice at P8 and P15. (n = 16-18 mice/-sex/genotype, p values shown are from unpaired t tests)
(D-E) Histogram showing the difference in number of USV calls falling into each repertoire unit sorted from shortest calls to longest calls on the x axis.
(F-G) Quantification of Male and Female pup weights from Control and IL34 KO mice at P8 and P15. (n = 16-18 mice/sex/genotype, two-way ANOVA age x genotype, p values shown in legend are main effect of genotype).
(H) Quantification of total distance moved over a ten-minute period in the open field. (n = 10-16 mice/sex/genotype, two-way ANOVA sex x genotype, p value showin in legend is main effect of genotype).
(I) Quantification of social behavior from the three-chamber sociability assay. (n = 10-16 mice/sex/genotype, two-way ANOVA sex x genotype, p value showin in legend is main effect of genotype).
(J-K) Quantification of performance (trial time and errors) of male Control and IL34 KO mice in the barnes maze across three training days and two reversal learning days. (n=8 male mice/genotype, two-way ANOVA day x genotype, p values shown in legend are main effect of genotype, significance of errors on reversal day 1 from Sidak's *post-hoc* test).
All data are mean ± s.e.m. p-values that fall below p<0.05 are denoted with an asterisk.

Supp. Figure 6

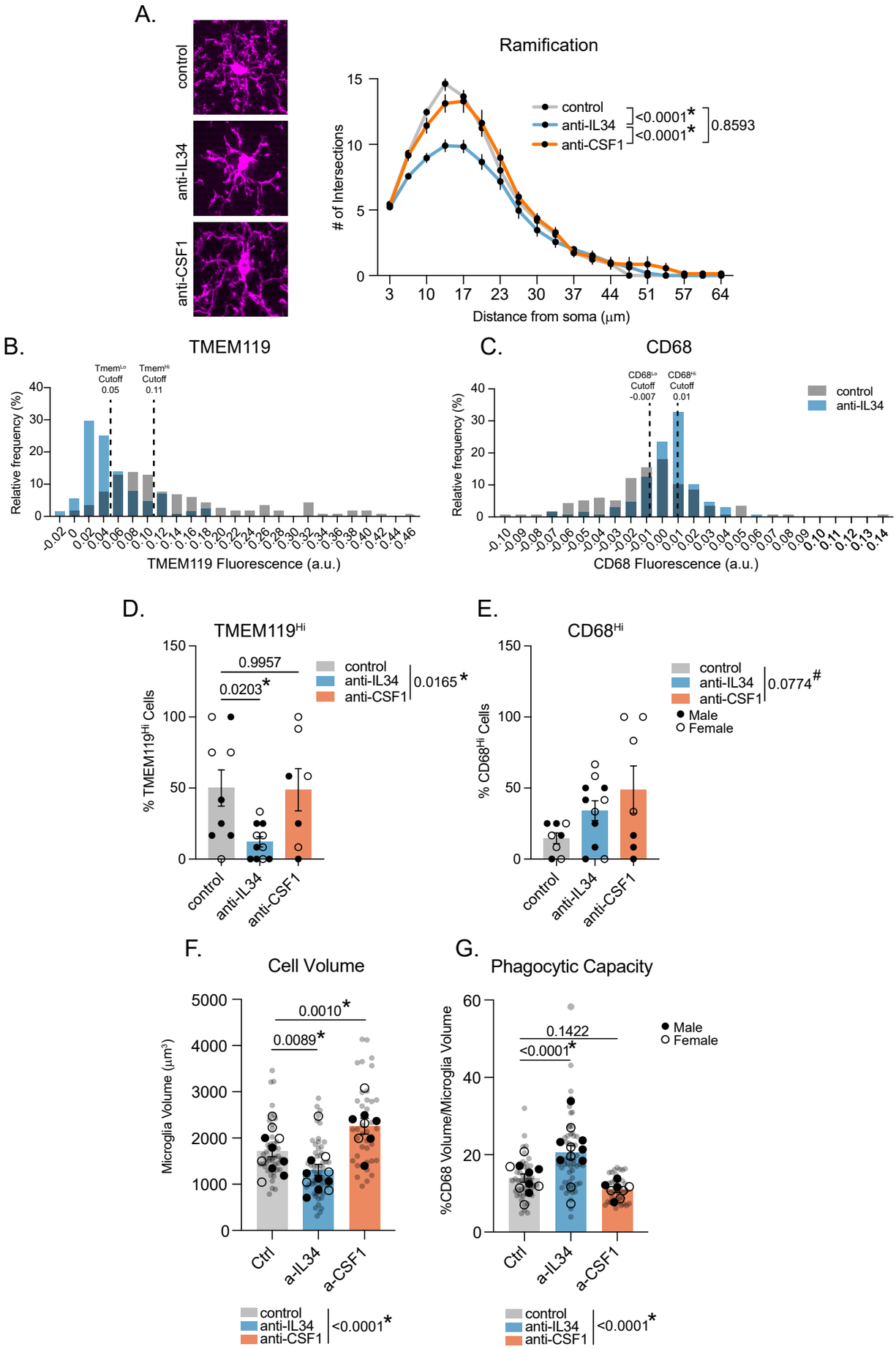

Supp. Figure 7

Supplemental Figure 7. IL34 blocking reduces microglial ramification, impacts % TMEM^{Hi} and CD68^{Hi} cells, decreases cell volume, and increases phagocytic capacity

(A) Representative images of individual microglia (Iba1) and sholl analysis quantification of cell ramification from anterior cingulate cortex of control, anti-IL34, and anti-CSF1 mice. (n = 5-8 mice/sex/treatment, 6 cells analyzed per mouse, two-way ANOVA distance from soma x genotype, p values shown are main effect of genotype).

(B-C) Histograms of relative fluorescence of TMEM119 and CD68 stain within individual microglia.

(D-E) Quantification of TMEM119^{Hi} and CD68^{Hi} microglia from control, anti-IL34, and anti-CSF1 mice. (n = 3-6 mice/sex/antibody, data shown are a percentage of 12 cells measured per animal across 3 images, one-way ANOVA, p values shown over bars are from Sidak's *post-hoc* test, main effect of antibody shown in legend).

(F-G) Quantification of microglial cell volume and phagocytic capacity. (n = 3-5 mice/sex/antibody, 4-6 cells analyzed per mouse, 141 cells total, individual microglia represented by gray circles, animal averages represented by black dots, nested one-way ANOVA, p values shown are from Sidak's *post-hoc* test, main effect of antibody shown in legend).

All data are mean ± s.e.m. p-values that fall below p<0.05 are denoted with an asterisk, and p-values between 0.05 and 0.10 denoted with a #.

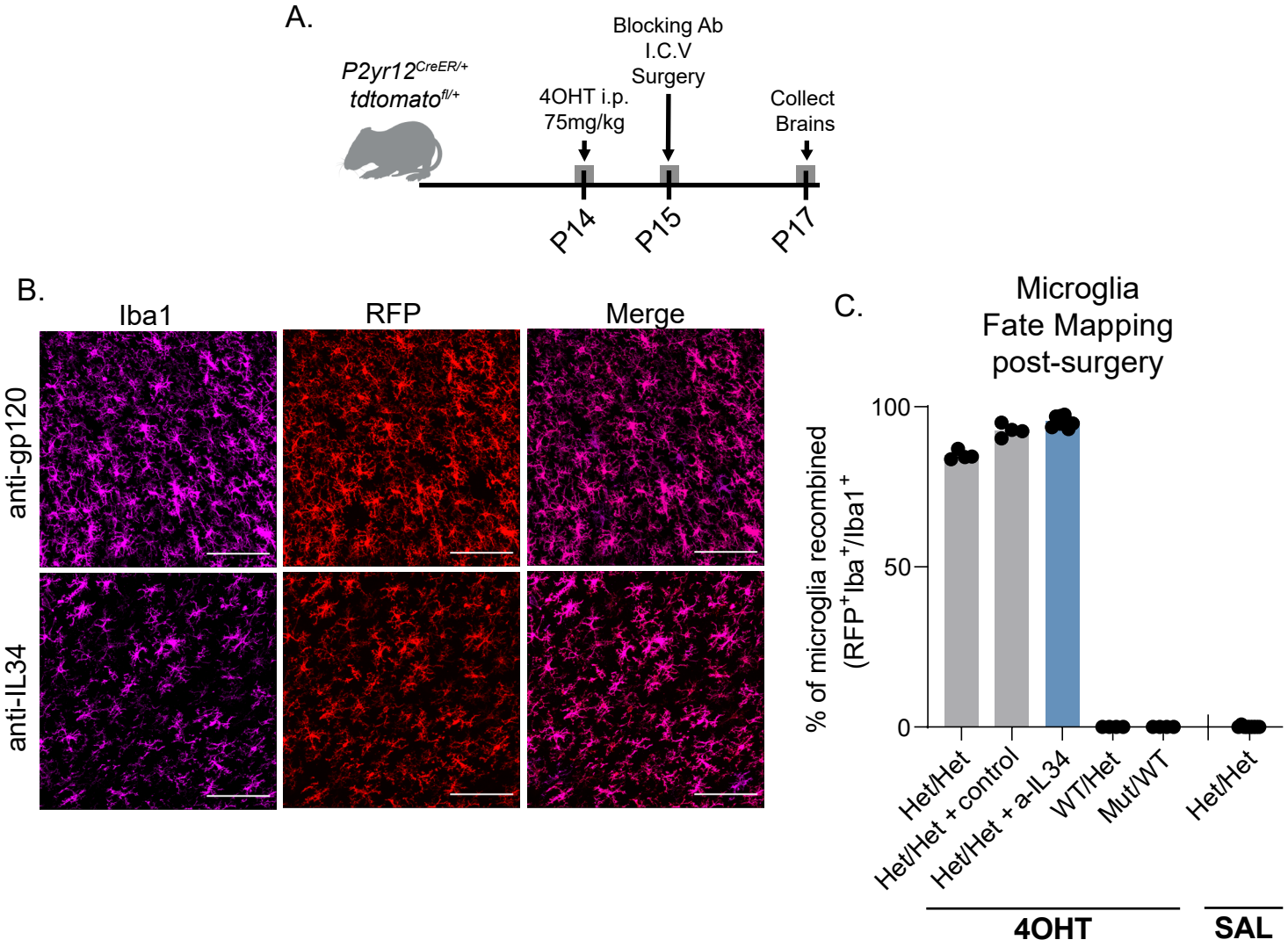

Supplemental Figure 8. anti-IL34 treatment does not cause mass microglial death and repopulation
(A) Experimental schematic of 4-hydroxytamoxifen injection , blocking antibody surgery, and tissue collection.
(B) Representative images of Iba1 and RFP staining in the ACC of mice treated with either the control or anti-IL34 blocking antibody.
(C) Quantification of the percentage of microglia (total Iba1+ cells) that were also RFP+ following blocking antibody administration.

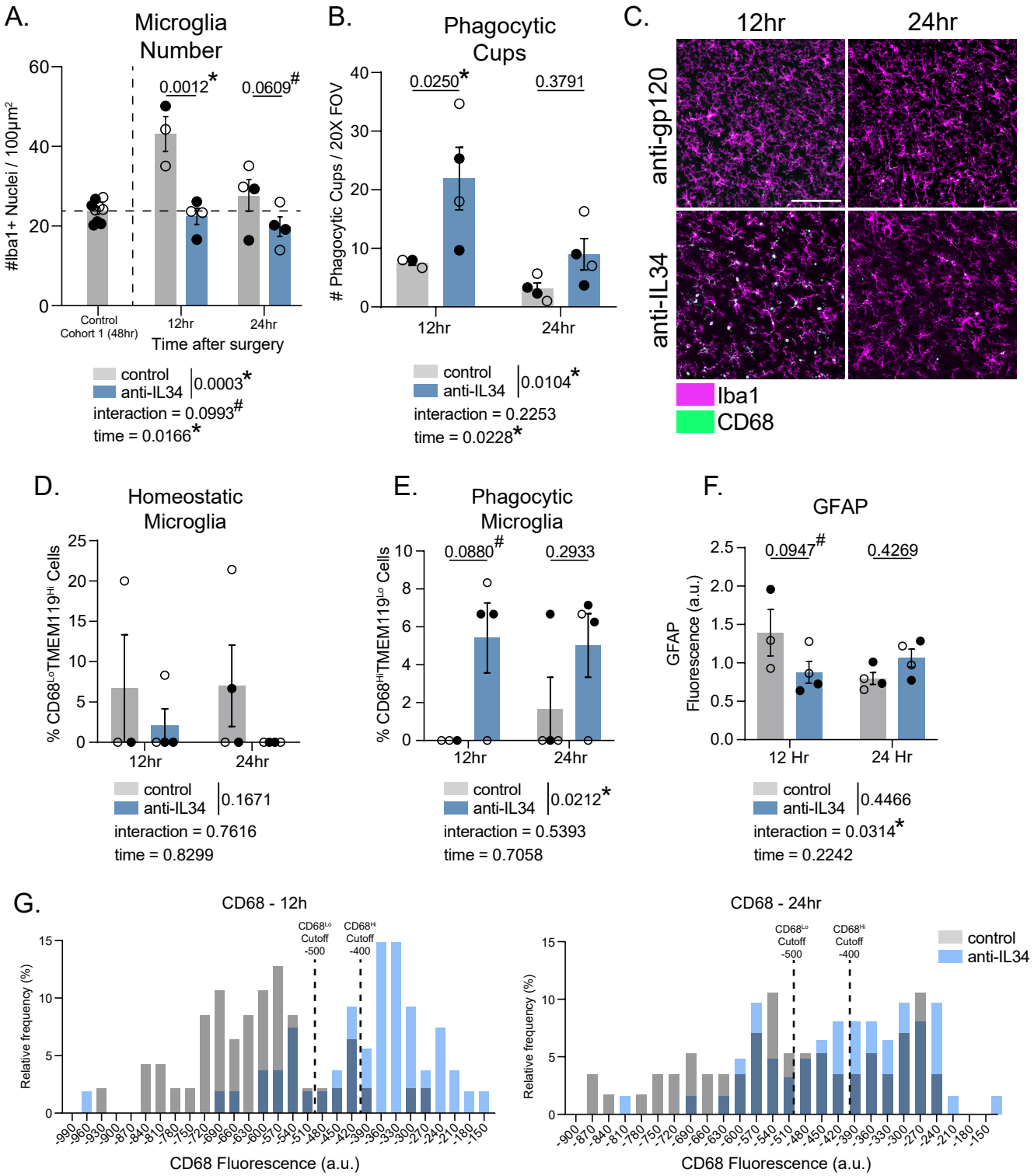

Supplemental Figure 9. Surgery causes microglial proliferation that is blunted by anti-IL34 and anti-IL34 increases phagocytic microglia
(A) Quantification of microglia number in mice treated with a control or anti-IL34 blocking antibody 12 and 24 hours following surgery. Microglia number from controls from the original cohort collected 48 hours post-surgery is also shown. (n = 3-4 mice/timepoint/antibody, data shown are an average of three images taken from 3 sections of each mouse, two-way ANOVA, p values shown are from Sidak's *post-hoc* test, main effect of antibody and timepoint and interaction effect shown in legend).
(B) Quantification of the number of phagocytic cups within a 20X field-of-view. (n = 3-4 mice/timepoint/antibody, data shown are an average of three images taken from 3 sections of each mouse, two-way ANOVA, p values shown are from Sidak's *post-hoc* test, main effect of antibody and timepoint and interaction effect shown in legend).
(C) Representative images of Iba1 and CD68 staining in mice treated with a control or anti-IL34 blocking antibody 12 and 24 hours following surgery.
(D-E) Quantification of $CD68^{Lo}TMEM119^{Hi}$ homeostatic microglia and $CD68^{Hi}TMEM119^{Lo}$ phagocytic microglia in all four groups. (n = 3-4 mice/time-point/antibody, data shown are a percentage of 12 cells measured per animal across 3 images, two-way ANOVA, p values shown are from Sidak's *post-hoc* test, main effect of antibody and timepoint and interaction effect shown in legend).
(F) Quantification of GFAP mean gray value in all four groups. (n = 3-4 mice/timepoint/antibody, data shown are an average of four images taken from 4 sections of each mouse, two-way ANOVA, p values shown are from Sidak's *post-hoc* test, main effect of antibody and timepoint and interaction effect shown in legend).
(G) Histograms of relative fluorescence of CD68 stain within individual microglia at both timepoints.
All data are mean ± s.e.m. p-values that fall below p<0.05 are denoted with an asterisk, and p-values between 0.05 and 0.10 denoted with a #.